



Effect of Quenching and Partitioning on Microstructure and Mechanical Properties of High-Carbon Nb Microalloyed Steel

I. DEY, R. SAHA, B. MAHATO, M. GHOSH, and S.K. GHOSH

In this study, high-carbon Nb microalloyed hot rolled steel plates are subjected to quenching and partitioning (Q&P) treatment at different temperatures and time durations. Dilatometry results show that increasing cooling rate (CR) leads to suppression of transformation start and finish temperatures of high-temperature transformation products like pearlite (P) or bainite (B), whereas martensite (M) transformation triggers with increasing cooling rate from 5 to 50 °C/s. The observations made by optical (OM), scanning (SEM), and transmission electron microscopy (TEM) reveal mixed-phase microstructures consisting of preformed/tempered martensite (PTM), retained austenite (RA), twin martensite (TM), and lower bainite (LB) for the isothermally heat-treated (IHT) samples subjected to Q&P at 200 °C and 180 °C for 30 minutes. The maximum volume percentage of RA (V_γ) and C content in RA (C_γ) is witnessed in the IHT samples subjected to Q&P for 30 minutes at 200 °C and 180 °C, respectively, followed by the hot rolled air-cooled (HRAC) sample. The formation of very fine NbC precipitates (~17 to 33 nm) is also evident in HRAC and Q&P at 160 °C for 30 minutes samples, which are expected to contribute significantly to precipitation strengthening. Hardness shows an increasing trend from 36 HRC to 65 HRC with increasing CR from 0.5 to 50 °C/s. The best combinations of the ultimate tensile strength (UTS) and total elongation (TEL) in Q&P 200 samples (36043 MPa pct) followed by Q&P 180 samples (32759 MPa pct) can be correlated with their higher values of V_γ and C_γ .

<https://doi.org/10.1007/s11661-024-07431-7>

© The Minerals, Metals & Materials Society and ASM International 2024

I. INTRODUCTION

HIGH-CARBON steels (HCS) are widely used for making high-quality tire cords, tire bids, rail lines, tee-rails, suspension bridge cables, hoses, conveyor belts, etc., due to excellent combinations of strength and ductility.^[1,2] Microalloying additions of elements like Nb, V, and Ti in HCS increase their performance because these elements are beneficial to restrict the

austenite grain growth by solute drag or precipitation pinning mechanisms, thereby resulting in the finer transformation products during industrial thermomechanical controlled processing (TMCP).

The development of high-strength low alloy microalloyed steels with a higher yield strength (YS) than conventional carbon–manganese (C–Mn) steels was witnessed in the past few decades. Later, the development of 1st generation advanced high-strength steels (AHSS) was aimed to achieve higher strength without sacrificing the ductility. This family included dual phase (DP), complex phase (CP), ferrite-bainite (FB), martensitic (MS or MART), high-strength low alloy (HSLA), transformation-induced plasticity (TRIP), hot-formed (HF) steels, etc. These steels primarily exhibited ferrite (F) and bainite/martensite (B/M) microstructures. In the next era, the 2nd generation AHSS, such as twinning-induced plasticity (TWIP) steels with parent austenite (γ) matrix, were developed, exhibiting improved combinations of strength and ductility. Afterward, the 3rd generation AHSS like quenching and partitioning (Q&P) steels, TRIP-aided bainitic ferrite steels with excellent combinations of strength (1000 to 1500 MPa), and formability have been developed to meet the ever-rising demand of lightweight components for the

I. DEY is with the Department of Metallurgy and Materials Engineering, Indian Institute of Engineering Science and Technology, Shibpur, Howrah, 711103, India and also with the Product Development Group, R & D Department, Jindal Steel and Power Limited, Raigarh, 496001, India. R. SAHA is with the Product Development Group, R & D Division, Tata Steel Limited, Jamshedpur, 831007, India. B. MAHATO and M. GHOSH are with the Materials Engineering Division, CSIR-National Metallurgical Laboratory, Jamshedpur, 831007, India. S. K. GHOSH is with the Department of Metallurgy and Materials Engineering, Indian Institute of Engineering Science and Technology, Shibpur, Howrah, 711103, India. Contact e-mail: skghosh@metal.iiests.ac.in.

Manuscript submitted December 6, 2023; accepted April 29, 2024.

Article published online May 27, 2024

reduction of greenhouse gasses.^[3,4] Further improvements of the mechanical properties can be done by creating a microstructure consisting of M and carbon-enriched RA because, during straining, steels containing a significant amount of RA gradually transform to M with a subsequent increase in strain hardening rate, thereby exhibiting a superior combination of strength and toughness. The novel Q&P process was first developed by Speer *et al.*, which included complete/partial austenitization followed by quenching below the martensite start temperature (M_s) and subsequent isothermal holding (IH) between M_s and martensite finish temperature (M_f) to allow adequate carbon diffusion from supersaturated M to untransformed γ to stabilize significant amount of γ at RT.^[4,5] Although G. Mandal *et al.* witnessed that before Q&P, samples subjected to full austenitization at reasonably higher temperatures than the partially austenitized samples revealed more RA at RT.^[6]

It has been recognized that retention of γ at RT is reliant on the initial quench temperature (T_Q), partitioning temperature (T_P), and time (P_t). There are possibilities that during final cooling to RT, some γ can also transform to high-carbon secondary M (SM) depending on the C enrichment in γ .^[7] This untempered SM exhibits higher hardness than the preformed M (PM) due to its higher C content.^[8] During partitioning, other microstructural changes can also occur, which include tempering of PM, precipitation of carbides, and formation of B.^[9–11] It is already reported that M can also trigger the B formation below M_s .^[12] The formation of carbide during Q&P for HCS is undesirable for stabilizing γ at RT, and to avoid this, the rule of thumb is the addition of carbide-suppressing elements like Si and/or Al in more amounts.^[3,4,11,12] Adding Si can effectively suppress carbide formation as it acts as a graphitizer. However, it is not possible to completely suppress the formation of transitional carbides (ϵ/η) during subsequent partitioning by increasing Si content, and this could be a convincing reason for not acquiring the equivalent amount of RA estimated by thermodynamic simulations. Conflictingly, some researchers have also argued that Si enhances the formation of transitional carbides. Pierce *et al.* and Hajyakbari *et al.* have reported that precipitation of ϵ/η carbides occurs in conjunction with partitioning for 0.38–1.48Si and 0.3–1.6Si (wt pct) steels, respectively.^[8,11,13] Kim *et al.* have concluded that carbide precipitation can occur regardless of high Si content. However, the degree and kinetics can be controlled by increasing the Si content to 2 wt pct for a 1 wt pct C steel.^[14] Although increasing C content can indeed lower M_s significantly and thereby stabilize more γ at RT, with increasing P_t , the chances of carbide formation and carbide coarsening also increase for HCS.^[11,12] On the contrary, shorter P_t is also not favorable for large-scale industrial steel components production since temperature uniformity is hard to achieve in this case. Nevertheless, during Q&P, suppression of other high-temperature transformation products like ferrite (F), pearlite (P) and/or bainite (B) is also necessary, for which effective addition of alloying

elements like Mn (γ stabilizer) and Si is required which not only provides adequate hardenability but also eradicates the chances of formation of these phases during quenching.^[4] Furthermore, microalloying additions of Nb, V etc., are beneficial to achieve additional strengthening by grain refinement (solute drag or particle pinning) and precipitation hardening. It has been reported that these elements can lead to the pancaking of austenite grains during HR, leading to a more uniform and refined final microstructure by increasing the volume fractions of RA and other low-temperature transformation constituents.^[15–17]

In view of the above, it can be said that the knowledge of the Q&P applied to HCS is limited in the literature.^[4,12] Using alloying elements like Mn and Si in higher amounts to stabilize significant amounts of RA at RT and hinder undesirable carbide formations for such high C content, respectively, is also limited.^[4,18] Nevertheless, S. S. Nayak *et al.* have investigated the role of Si in the suppression of carbide formation during a two-step Q&P process for 1.01C steel by varying the Si content from 1.54 to 2.03 wt pct and concluded that lower quench temperature is beneficial for stabilizing more RA at RT.^[4] However, the high Cr (≈ 1.46 wt pct) promotes harmful cementite during spheroidization, which further reduces the ability of HCS to sufficient C partitioning.^[4] Both one and two-step Q&P are well documented in the literature.^[4–19] During one-step Q&P, T_Q and T_P are the same whereas, for two-step Q&P, T_P is usually higher than T_Q to allow C partitioning at higher temperatures. Hence, later, it is also known as the quenching–partitioning–tempering (Q–P–T) process. It is noteworthy that one-step Q&P does not need additional tempering and is more suitable for industrial large-scale production in terms of energy-saving and cost-effectiveness. It is also true that more alloying elements are not desirable in terms of cost-effectiveness. Another study by J. Zhang *et al.* have shown that quenching at 170°C followed by partitioning at 400°C and tempering at the same partitioning temperature for 600 s results in 24 pct RA for a Fe-0.67C-1.48Mn-1.53-Si-0.038Nb steel.^[18] In a previous study, I. Dey *et al.* have already reported that a significant amount of RA was not stabilized at RT after single step Q&P at 200°C for a Fe-0.66C-0.67Mn-0.20Si-0.03Nb steel, which may be attributed to insufficient Mn and Si contents.^[19] It has been reported earlier that partitioning at 400 °C for 40 seconds triggered the γ /M interface migration, and consequently, the volume fraction of RA at RT was significantly reduced for 0.2C-1.59Mn-1.63Si steel, as this movement direction is from M to γ .^[20] In contrast, Nb can effectively retard this interface migration due to its well-known solute drag or precipitation pinning effect.^[20] Moreover, the consequences of carbide forming microalloying elements like Nb, are well known to boost the mechanical properties by precipitation strengthening instead of Q&P, are also currently lacking. Hence, the objective of the present study is to design a novel Nb microalloyed HCS to achieve excellent mechanical properties by optimizing two key parameters. First, increasing the content of Mn and Si while

keeping the concentrations of C and other alloying elements almost the same as reported earlier^[19] and second, appropriate selection of Q&P temperature and time at which the maximum volume percentage of RA can be stabilized at RT.

II. EXPERIMENTAL PROCEDURES

In this study, high-carbon Nb microalloyed forged bar, having a cross-sectional area of $\approx 280 \times 175 \text{ mm}^2$ and designated as HC9 with chemical composition given in Table I, was procured from Tata Steel, Jamshedpur, India. Higher amounts of Mn and Si are added to suppress the pearlite (P) transformation as Mn is an austenite stabilizer and Si is a graphitizer, inhibiting the harmful carbide precipitation during partitioning as the C content in the present steel is relatively high (0.68 wt pct), which results in effective C partitioning to RA. A decent ratio of Mn and Si is expected to stabilize enough retained austenite (RA) at room temperature (RT). Initially, the various phase transformation temperatures and volume percentage of different phases at respective temperatures were estimated from Thermo-Calc[®] in conjunction with the TCFE9 database software, whereas continuous cooling transformation (CCT) and time-temperature-transformation (TTT) diagrams for the present composition were estimated by using suitable empirical equations as well as JMatPro[®] software. After proper selection of the parameters required for experimental design, these forged bars ($\approx 30 \text{ mm}$ thickness) were first homogenized at $1200 \text{ }^\circ\text{C}$ for 1 h in a high-temperature muffle furnace and then subjected to hot rolling (HR) with finish rolling temperature (FRT $\approx 1000 \text{ }^\circ\text{C}$) followed by air cooling (AC) to room temperature (RT). Here, $\approx 75 \text{ pct}$ hot deformation was given at several stages and an optical pyrometer was used to monitor the temperature of HR specimens at different rolling steps. In industrial practice, usually more than 75 pct hot deformation was given in several passes due to the higher capacities of industrial rolling mills, which was restricted under the current laboratory facilities. This HRAC was intentionally applied to simulate the industrial HR conditions to understand the effect of HR followed by free AC on the microstructural constituents, especially whether any RA can be stabilized after only HRAC due to the higher content of Mn and Si in the present steel and to compare these results with those estimated from JMatPro[®] software.

For the dilatometry study, cylindrical specimens with lengths and diameters of $\approx 71 \text{ mm}$ and $\approx 6 \text{ mm}$, respectively, were prepared by machining from the hot rolled plates ($\approx 8 \text{ mm}$ thickness). A Gleeble 3800 simulator with an electrical resistance heating facility was utilized

for the dilatometry study. A thermocouple welded on the specimen surface midway between two ends was used for monitoring the temperature of the sample. These cylindrical samples were first heated to $1050 \text{ }^\circ\text{C}$ at a heating rate of $5 \text{ }^\circ\text{C/s}$ followed by soaking for 3 minutes, then subjected to continuous cooling (CC) to RT at different cooling rates (CRs) ranging from 0.5 to $50 \text{ }^\circ\text{C/s}$. It needs to be mentioned that continuous cooling (linear) is different from free cooling (nonlinear). In industry, thermomechanical controlled processing (TMCP) consists of thermomechanical controlled rolling (TMCR) followed by accelerated cooling (ACC). In the present study, the parameters for TMCP, like temperatures and heating and cooling rates, are chosen to simulate the industrial HR process for producing long products like wire rods. A different set of hot rolled steel plates were subjected to quenching and partitioning (Q&P) treatments. These HRAC samples were first austenitized at $900 \text{ }^\circ\text{C}$ for 45 mins, followed by AC to three different temperatures of $200 \text{ }^\circ\text{C}$, $180 \text{ }^\circ\text{C}$, and $160 \text{ }^\circ\text{C}$ and then subsequent isothermal holding (IH) for 30 mins in a salt bath furnace (SBF) maintained at these 3 mentioned temperatures followed by AC to RT. Another set of samples was subjected to IH at $200 \text{ }^\circ\text{C}$ in a salt bath furnace for different time durations of 15 minutes, 1 and 5 hours, respectively, followed by AC to room temperature. Both these processes involving Q&P for various temperature and time variations are illustrated in Figures 1(a) and (b), respectively. These time variation steps were applied only at $200 \text{ }^\circ\text{C}$ and not for the other two temperatures since it was the closest temperature of measured M_s from empirical formula for the present composition and dilatometry results, as discussed in sections A (Table II) and B.1, respectively.

Small samples were cut and mechanically polished by following standard metallographic sample preparation practices like polishing with SiC emery papers up to grit size of 2000 followed by coarse (cloth) and fine polishing with a diamond paste up to $1 \text{ }\mu\text{m}$. These samples were then etched with 2 pct nital solution to observe the microstructures under a Carl Zeiss, Axiovert 40 Mat optical microscope, a Hitachi scanning electron microscope (SEM, S-3400N), and a high-resolution energy-filtered transmission electron microscope (TEM, JEOL JEM 2200FS) with an operating voltage of 200 kV . Before the TEM study, disc samples with a diameter of 3 mm were cut from the thin foils and subsequently polished using a twin jet electropolishing (Struers TenuPol-5) containing an electrolyte solution of 90 pct CH_3COOH and 10 pct HClO_4 . Reliable ImageJ software was used to calculate average volume fractions of pearlite in HRAC sample and 10-15 OM and SEM micrographs were chosen for this purpose. X-ray diffraction studies of HRAC and HT samples were

Table I. The Chemical Composition and A_{c1} and A_{c3} Temperatures of the Investigated Alloy (Wt Pct)

Alloy Code	C	Mn	Si	Nb	S	P	Fe	A_{c1} ($^\circ\text{C}$)	A_{c3} ($^\circ\text{C}$)
HC9	0.68	1.72	2.20	0.036	0.008	0.012	Bal.	720	836

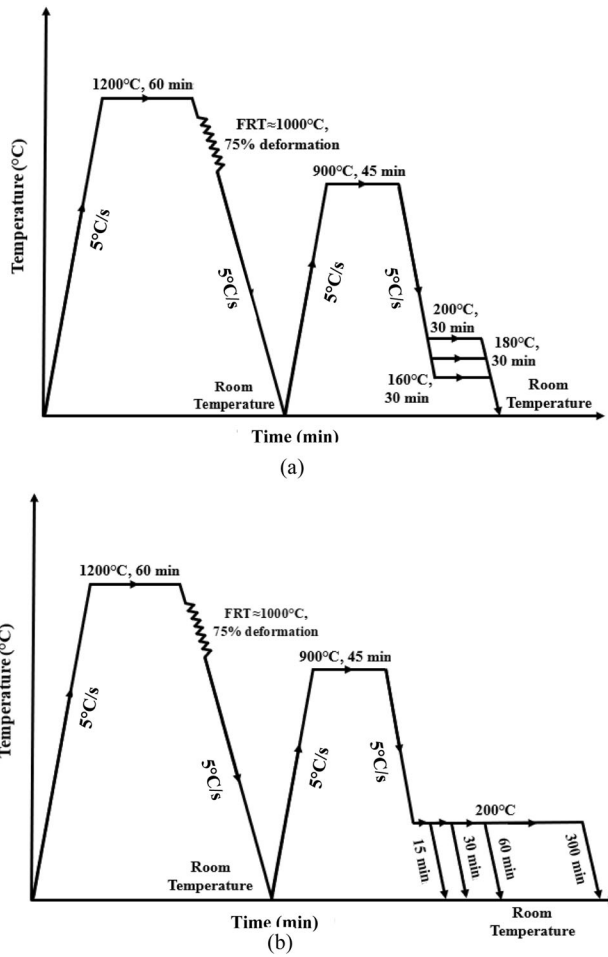


Fig. 1—Schematic representation of (a) and (b) hot rolling and heat treatment schedules with varying temperature and time, respectively.

carried out using a Bruker Advance D8 X-ray diffraction machine integrated with a copper tube ($\text{CuK}\alpha$) with an operating voltage of 40 kV and a current of 40 mA. The XRD raw data were collected over a 2θ range of 35 to 105 deg with a step size of $0.02^\circ/\text{s}$. The raw diffraction data were then analyzed using Panalytical X'pert High Score Plus and DIFFRAC.TOPAS software and, consequently, the Rietveld refinement method was utilized to evaluate the volume fractions of RA (V_r).

The Rockwell hardness values in the C scale (HRC) were measured in a Rockwell hardness testing machine. Sub-sized tensile specimens with a gauge length of 25 mm were prepared by machining following the ASTM E8M-2016 standard. Tensile tests were performed in a 50 kN uniaxial universal tensile testing machine (Instron 5900R) with a crosshead velocity of 0.5 mm/min and a precision strain measuring extensometer attached.

III. RESULTS AND DISCUSSION

A. Calculation of Phase Transformation Temperatures Using JMatPro[®] Software

Figures 2(a) and (b) display continuous cooling transformation (CCT) and time–temperature–transformation (TTT) diagrams, respectively, estimated from JMatPro[®] software. It can be seen from Figure 2(a) that when the cooling rate is between 1 and $10^\circ\text{C}/\text{s}$, the expected microstructure is mainly pearlite and martensite while cooling continuously from the austenite region, whereas the TTT diagram in Figure 2(b) indicates that isothermal holding only below the martensite start temperature ($M_s \approx 171^\circ\text{C}$) will result in a fully martensitic microstructure. The relationship between critical phase transformation temperatures and corresponding phase fractions was also estimated before the experiment using Thermo-Calc[®] software, as shown in Figure 2(c). The austenite start (A_{c1}) and finish (A_{c3}) temperatures are 728°C and 756°C as indicated in Figure 2(c).

JMatPro[®] is a well-known and reliable cross-platform software which is used for the calculations of TTT and CCT diagrams, physical, thermophysical and high-temperature mechanical properties, Jominy hardenability, etc., based on the physical models for multicomponent alloys. It is simply a user-friendly software that requires only chemical compositions, austenitizing temperature, and austenite grain size as inputs for these broad ranges of materials properties calculations. Here, the thermodynamic module first computes the critical phase transition temperatures by using appropriate empirical formulae and finally the software calculates the time taken for these transformations based on Johnson–Mehl–Avrami equation.^[21–23] This TTT diagram can be further converted to a CCT diagram using Scheil's Additivity Rule.^[21,24] In this connection, the calculation of CCT and TTT diagrams for any steel chemistry can also be done by using the model developed by Kirkaldy *et al.*, as shown by Eqs. [1] through [3].^[25,26] Later, Li *et al.* modified the Equations of Kirkaldy model to improve the accuracy of the existing model, as shown here by Eqs. [4] through [6].^[27]

$$\tau(x, T) = \frac{1}{\alpha(N)D_{eff}\Delta T^q} \int_0^x \frac{dx}{x^{\frac{2(1-x)}{3}}(1-x)^{\frac{2q}{3}}} \quad [1]$$

$$\tau_{TTT} = \frac{1}{2^{(N/8)}(\Delta T)^3} e^{\left(\frac{Q_{eff}}{RT}\right)} \sum_{j=1}^m \alpha_j C_j \quad [2]$$

$$\tau_{0.1\text{pct}} = \frac{\exp\left(\frac{2000}{T}\right)}{2^{\left(\frac{N}{8}\right)}(Ae_3 - T)^3} (60\text{C} + 90\text{Si} + 160\text{Cr} + 200\text{Mo}) \quad [3]$$

Table II. Calculated Transformation Temperatures of HC9

Calculated Transformation Temperatures	Ac ₁ (°C)	Ac ₃ (°C)	B _s (°C)	M _s (°C)
Empirical Equations	754	798	392	215
Thermo-Calc [®] and JMatPro [®]	728	756	420	171

$$\tau(x, T) = \frac{F(C, Mn, Si, Ni, Cr, Mo, G)}{\Delta T^n \exp(-\frac{Q}{RT})} S(X) \quad [4]$$

$$S(X) = \int_0^x \frac{dx}{x^{0.4(1-x)}(1-x)^{0.4X}} \quad [5]$$

$$X = \int_0^x \frac{\Delta T^n \exp(-Q/RT) x^{0.4(1-x)}(1-x)^{0.4X}}{F(C, Mn, Si, Ni, Cr, Mo, G)} dt \quad [6]$$

$$Ac_1 = 754.83 - 32.25C - 17.76Mn + 23.32Si + 17.3Cr + 4.51Mo + 15.62V \quad [7]$$

$$Ac_3 = 937.3 - 224.5\sqrt{C} - 17Mn + 34Si - 14Ni + 21.6Mo + 41.8V - 20Cu \quad [8]$$

$$B_s = 656 - 57.7C - 35Mn - 75Si - 15.3Ni - 34Cr - 41.2Mo \quad [9]$$

$$M_s = 525 - 350(C - 0.05) - 45Mn - 30Cr - 20Ni - 16Mo - 5Si - 8W + 6Co + 15Al - 35(Nb + V + Zr + Ti) \quad [10]$$

here τ = time required for the transformation of x fraction of austenite at temperature T , $\alpha = \beta \times 2^{(N-1)/2}$, β is an empirical coefficient, N = Grain size (ASTM), D = Effective diffusion coefficient, ΔT = Undercooling below the Ae_3 temperature, where austenite is unstable, q = Exponent, which depends on effective diffusion, α_j = Constant for element j , C_j = Concentration of element j , Q_{eff} = Effective activation energy for diffusion, F = Function of steel composition in wt pct, G = Prior austenite grain size (ASTM), n = Exponent of undercooling, $S(X)$ = Reaction rate term, *i.e.*, an approximation of the sigmoidal effect of phase transformation, X = Amount of phase transformation under arbitrary cooling conditions.

Table II shows various transformation temperatures estimated for the present composition by using empirical formulas and thermodynamic simulation software. Here, Ac_1 , Ac_3 , B_s , and M_s are the austenite start, austenite finish, bainite start, and martensite start temperatures, respectively. Equations [7] through [10] were used to calculate the various transformation temperatures.^[28] The predicted M_s in Table II is ≈ 44 °C higher than the JMatPro[®] results. It must be emphasized that the estimation of M_s strongly depends on initial prior austenite grain size (PAGS), which needs to be given as input while estimating both the CCT and TTT diagrams, as reported by Yang and Bhadeshia.^[29] Schulze *et al.* have also reported that phase transformation behavior is reliant on grain growth based on heating technique, austenitization temperature, and soaking time.^[30,31] Furthermore, the phase transformation kinetics is also dependent on the deformation conditions prior to cooling and due to this deformation, deformation-dependent diagrams D-CCT and D-TTT are already reported in the literature.^[31,32] It is also factual that the present database used in JMatPro[®] has some limitations of alloying element concentrations (e.g., Si < 1 wt pct).^[27]

B. Dilatometry Study

1. Cooling curves and continuous cooling transformation (CCT) diagram

Figures 3(a) through (f) display dilatation ($\Delta L/L_0$) versus temperature plots while cooling from the austenite region under different cooling rates from 0.5 to 50 °C/s. Table III lists the measured values of Ac_1 , Ac_3 , P_s , P_f , B_s , B_f , and M_s temperatures at each available cooling rate. It is visible from Figures 3(a) through (c) and Table III that with the increase in cooling rate (CR) (≈ 4.5 °C/s), the pearlite transformation start (P_s) and finish (P_f) temperatures are considerably lowered (≈ 70 °C and ≈ 73 °C, respectively), whereas the B_s and B_f temperatures decrease marginally (≈ 9 °C and ≈ 5 °C, respectively). It is also evident from Figures 3(c) through (f) and Table III that both the B_s and B_f temperatures decrease ≈ 17 °C and ≈ 20 °C, respectively, with the increasing CRs (≈ 45 °C/s) and thereafter, no traces of pearlite were found at comparatively higher CRs (> 5 °C) as evident from Figures 3(c) through (f). Higher deflection in the dilatation curves signifies a higher volume percentage of the transforming phases. It has already been reported that the addition of ≈ 0.03 wt pct Nb in C-Mn-Si steel can significantly reduce the ferrite transformation arena and lower the B_s temperature at higher cooling rates, which correlates well with the present study.^[33] B_s and M_s temperatures are determined from the dilatometric curve where the thermal contraction exhibits nonlinearity because of the volume expansion during bainite and the martensite

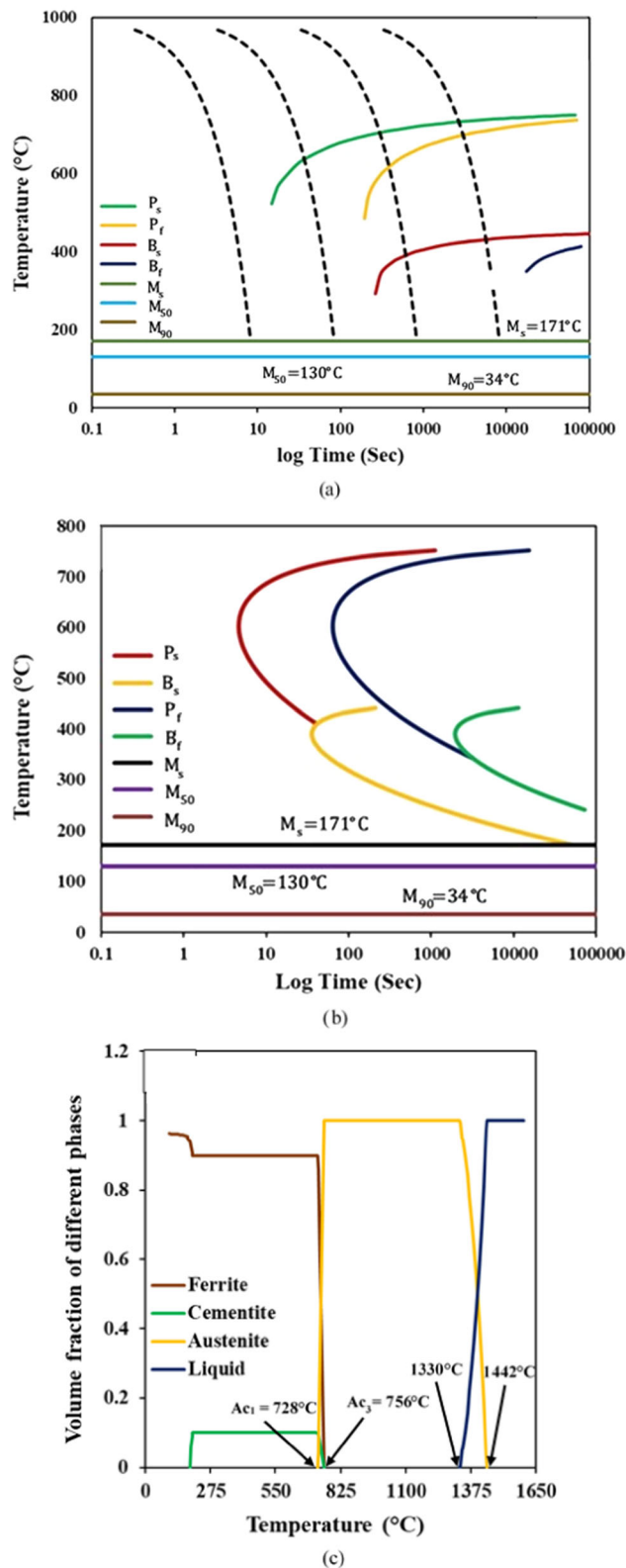


Fig. 2—(a) Continuous cooling transformation (CCT) and (b) time-temperature-transformation (TTT) diagrams estimated from JMatPro[®] software and (c) various phase fractions calculated from Thermo-Calc[®] software.

transformations, respectively. It is also evident from Figures 3(c) through (f) and Table III that, with the

increasing cooling rates from 5 to 50 °C/s, M_s also increases from 217 °C to 253 °C. This may be because at low cooling rates, more carbon atoms are being released from the octahedral sites of austenite (γ) and consequently, the additional driving force is required for martensite transformation, which results in low M_s temperature.^[34,35] However, some researchers have opined that at low cooling rates, the formation of diffusive transformation products like bainite, pearlite, or ferrite prior to martensite transformation assists carbon partitioning in γ , subsequently stabilizes the remaining γ and thereby lowers the M_s temperature.^[36] At higher cooling rates, some high-resolution dilatation curves exhibit minor splitting above the M_s , which may be correlated with carbide precipitations during cooling, as evident in Figures 3(c) through (f).^[37] Figure 3(g) shows the continuous cooling transformation (CCT) diagram and corresponding HRC values at each cooling rate. The reaction boundaries are also delineated on the CCT diagram to correlate the various phase transformation temperatures at different cooling rates. It can be seen from Figure 3(g) and Table III that both A_{c1} and A_{c3} temperatures vary marginally ($\leq 4^\circ\text{C}$) in all the cases because the heating rate was kept the same for all the cases ($\approx 5^\circ\text{C/s}$). The improved hardness value (≈ 29 HRC) with the increase of cooling rates from 0.5 to 50 °C/s indicates the formation of low-temperature transformation products like martensite (M) or bainite (B) in higher volume percentages.

2. Microstructure analysis of the dilatometry samples subjected to different cooling rates

Figure 4 reveals optical and SEM micrographs of HC9 steel processed through various cooling rates (CRs) from 0.5 to 50 °C/s. The respective HRC values are also shown in all the micrographs. It is evident from Figures 4(a) through (d) that a combination of mixed phases, mainly consisting of pearlite (P), bainite (B), and some amount of ferrite (F), is present in the final microstructures of the samples continuously cooled at a cooling rate of 0.5 and 1 °C/s, respectively. The pearlite nodules are delineated by yellow dotted lines. It is well known that the difference between resolved and unresolved pearlite (RP and URP, respectively) lies in the refinement of pearlite interlamellar spacing for the latter one. However, the presence of some amount of degenerated or pseudo pearlite (DP) is also evidenced by the increase in cooling rate from 0.5 to 1 °C/s [Figures 4(b) vis-à-vis 4(d)], which is an indication of insufficient carbon (C) diffusion during cooling. With the increase in CRs from 5 to 50 °C/s, the final microstructure is changed from martensite (M), bainite (B), and very little amount of pearlite (<5 vol. pct) at the grain boundaries to M and B primarily along with some carbide precipitates as shown by blue dotted circles and no traces of pearlite have been found at higher CRs as apparent from Figures 4(e) through (l). In this context, this change in microstructural constituents and formation of finer low-temperature transformation products at higher CRs are well reflected in the corresponding HRC values, which are significantly increased (32 HRC) with the increasing CRs from 0.5 to 50 °C/s. These observations

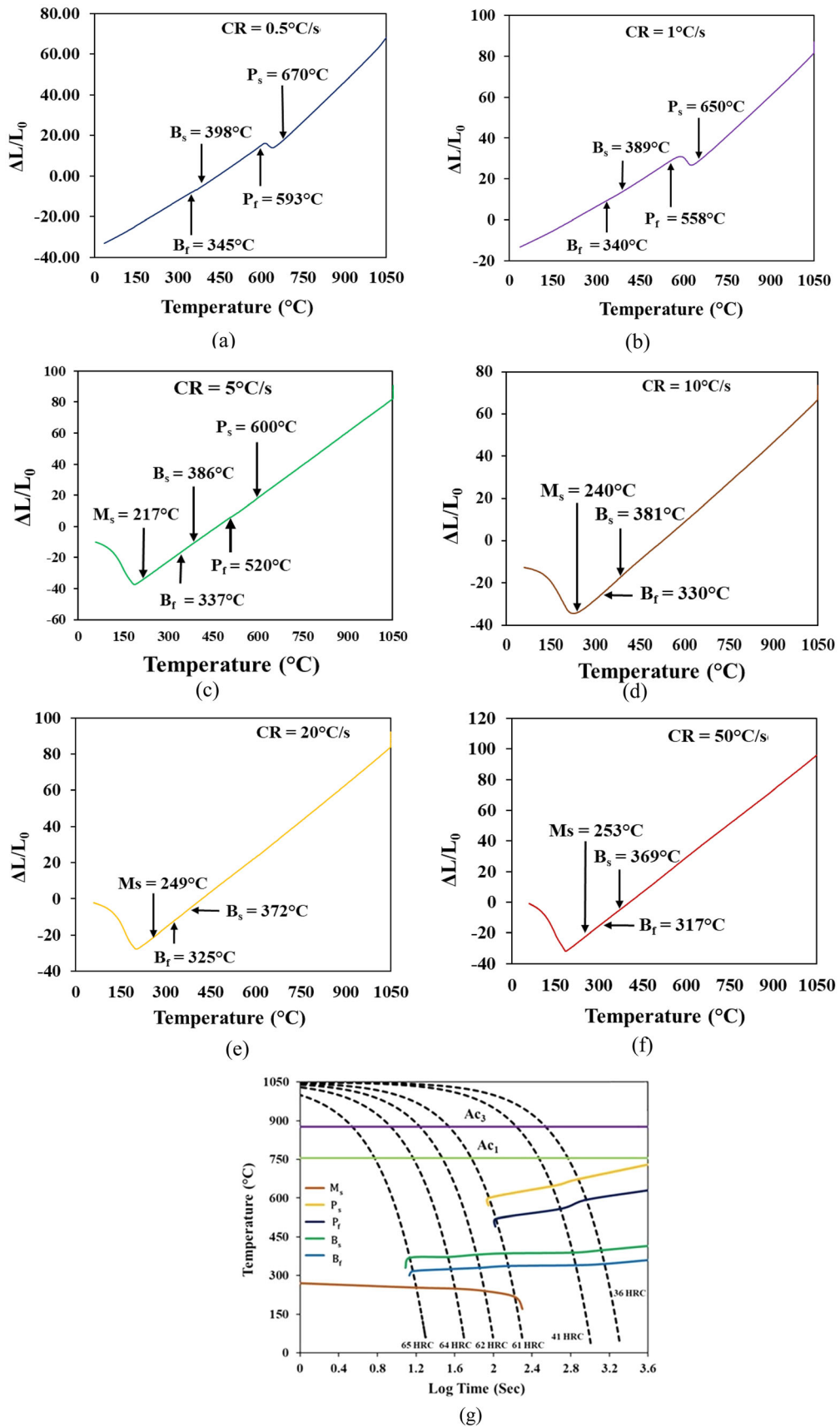


Fig. 3—(a) to (f) dilatometry plots under different cooling rates from 0.5 to 50 $^{\circ}\text{C}/\text{s}$, (g) Continuous cooling transformation (CCT) diagram determined from dilatometry results.

Table III. Transformation Temperatures of CCT Samples at Different Cooling Rates

Cooling Rates (°C/s)	A_{c1} (°C)	A_{c3} (°C)	P_s (°C)	P_f (°C)	B_s (°C)	B_f (°C)	M_s (°C)
0.5	754	877	670	593	398	345	—
1	755	877	650	558	389	340	—
5	756	873	600	520	386	337	217
10	752	874	—	—	381	330	240
20	753	875	—	—	372	325	249
50	755	877	—	—	369	317	253

match the dilatometry study, as discussed in Section B.1. The prior austenite grain boundaries (PAGB) are visible in the optical micrographs and for a better understanding, the PAGB is sketched by yellow dotted lines [Figure 4(e)]. It is also noticeable from Figure 4 that along with M and B, some amount of retained/untransformed austenite (RA) has also been observed. Zhao and Notis have reported that the formation of more volume percentage of diffusional constituents like F, P, or B before the M transformation stabilizes some amount of austenite by promoting the carbon partitioning in it and thereby lowers the M_s temperature for a 0.35C-1.4Mn-0.76Si-0.19Mo-0.07Cr-0.06Ni-0.16V steel, which is prominent at comparatively lower CRs [Figures 4(a) through (d)].^[38] On the contrary, Zhao and Notis have also mentioned that with the increase in CRs, M_s temperature will not vary markedly when M forms directly from austenite (γ) and no other mode of diffusional transformation occurs because the chemical composition of γ is not altered during undercooling in this case, which agrees with the present study [Figures 4(e) through (l)].^[38] Similar observations by Babasafari *et al.* have also concluded that the volume fraction of RA does not vary significantly with the increasing CR (≈ 155 °C) when M is the dominating phase for 1C-0.98Mn-0.18Cu-0.63Cr-0.21Si-0.09Ni-0.024Mo-Fe steel subjected to continuous cooling from an austenitizing temperature of 1000 °C.^[34] Nevertheless, it is also expected that at higher CRs along with M and B, some amount of γ will remain untransformed due to the presence of γ stabilizing elements like Mn and graphitizer like Si (inhibits cementite precipitation) in higher volume fractions in the present steel.

C. TMCP and Heat-Treated Samples

1. X-ray diffraction analysis

Figure 5 shows X-ray diffraction patterns of hot rolled, air-cooled, and heat-treated samples subjected to quenching and partitioning treatment (a) at different temperatures and (b) for different durations. The corresponding peaks of M and γ are also shown in these Figures. C contents in RA (C_γ) are calculated by using Eq. [11].^[39]

$$C_\gamma = \frac{a_\gamma - 3.547}{0.046} \quad [11]$$

Here, a_γ is the lattice parameter (Å) of RA, which was calculated using the Williamson–Hall method.^[40,41]

Table IV summarizes the values of V_γ and C_γ under different processing conditions. Here, T_P and P_t signify Q&P temperature (°C) and time (min), respectively. It can be seen from Figure 5(a) and Table IV that the highest amount of RA is obtained for the Q&P 200, followed by the Q&P 180 sample. Therefore, it can be said that despite the high C content in the present steel, the presence of a significant amount of Si (strong graphitizer) lowers the activity of C in γ at 200 °C and 180 °C, inhibiting/delaying the carbide formation and thereby allows C partitioning in γ during IH for 30 minutes which results in the stabilization of γ at room temperature. It is also apparent from Figure 5(a) and Table IV that for the HRAC sample, the values of both V_γ and C_γ are less than those Q&P 200 and Q&P 180 samples, which indicate that C partitioning from supersaturated M to γ occurs during holding for 30 minutes at these Q&P temperatures which were not possible for the HRAC sample subjected to direct cooling to RT after hot rolling. It is also evident from Figure 5(b) and Table IV that increasing partitioning time beyond 30 minutes results in a further decrease in both V_γ and C_γ values. In this regard, lower values of V_γ *i.e.*, < 1.5 and < 2 for Q&P 160 and Q&P 200_5 h samples, respectively, may be because C partitioning from supersaturated M to γ was not sufficient at a lower temperature of 160 °C in the former one, whereas for the latter one, excessive carbide formation may take place due to prolong holding at 200 °C because of higher C content in the current steel. Nevertheless, it cannot be overruled that the estimations of a_γ and C_γ are susceptible to significant errors due to the small intensities of the respective γ peaks in both samples.

2. Optical and SEM microstructures

Figures 6(a) and (b) show optical (OM) and SEM micrographs, respectively, of hot rolled and air-cooled (HRAC) samples with $FRT \approx 1000$ °C, which mainly reveals mixed-phase microstructure comprising of martensite (M), pearlite (P), and some amount of retained austenite (RA). It should be noted that after hot rolling, this sample was air cooled to RT at ≈ 5 °C/s from the γ regime, which is like the CR of the sample subjected to continuous cooling (CC) for the dilatometry study as discussed in Section B.2 [Figures 4(e) and (f)]. However, the continuously cooled samples,

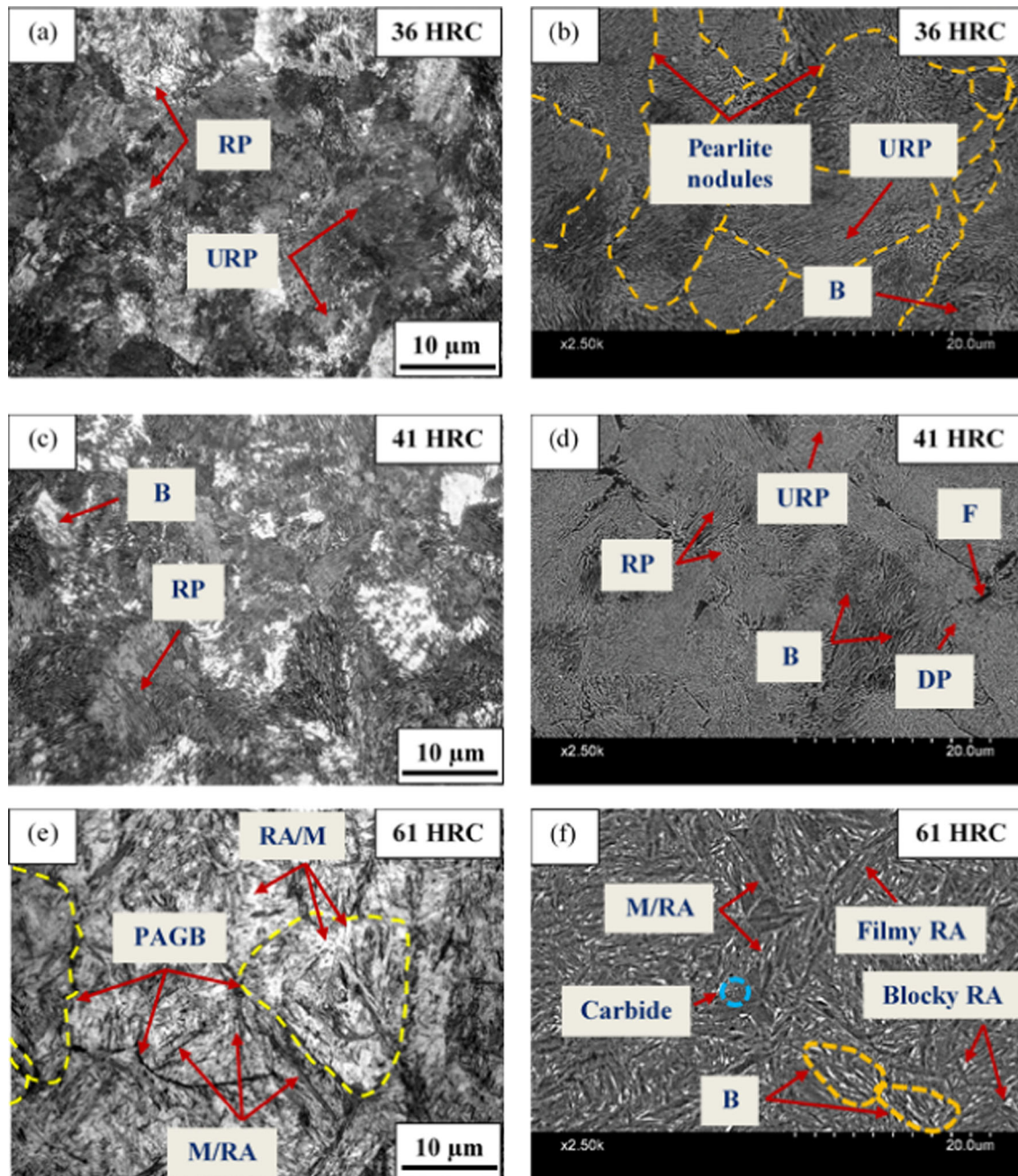


Fig. 4—Optical and SEM micrographs of the investigated steel processed through various cooling rates of (a) & (b) 0.5 °C/s, (c) (& d) 1 °C/s, (e) (& f) 5 °C/s, (g) (& h) 10 °C/s, (i) & (j) 20 °C/s, and (k) (& l) 50 °C/s. PAGB, RP, URP, DP, M, RA, B, and F are the abbreviations of prior austenite grain boundary, resolved and unresolved pearlite, degenerated pearlite, martensite, retained austenite, bainite, and ferrite, respectively.

prepared from HRAC steel plate, were further subjected to austenitization at 1050 °C at a heating rate of ≈ 5 °C/s followed by CC at different CRs to RT. Therefore, the history of deformation is expected to be lost in this case. The higher HRC value (≈ 5 HRC) and slightly higher volume fractions of P (≈ 0.05) at the grain boundaries in the HRAC sample compared to the continuously cooled sample under the same CR [Figures 4(e) and (f) vis-à-vis Figures 6(a) and (b)] may be attributed to the formation of finer recrystallized γ grains and thereby higher available grain boundary areas that act as preferable

nucleation sites for new grains, respectively, due to the applied ≈ 75 pct hot deformation and also nonlinearity of cooling for HRAC samples as discussed in section II. It is conventional that when the deformation temperature (T) is above the no recrystallization temperature (T_{nr}), then recrystallization of γ grains is the dominating mechanism, whereas when $T < T_{nr}$, pancaking of γ grains can be witnessed. Grain refinement is mainly associated with larger values of S_v *i.e.*, interfacial area of near planar crystalline defects like grain boundaries, deformation bands, etc. The values of S_v for $T > T_{nr}$ and $T < T_{nr}$ can

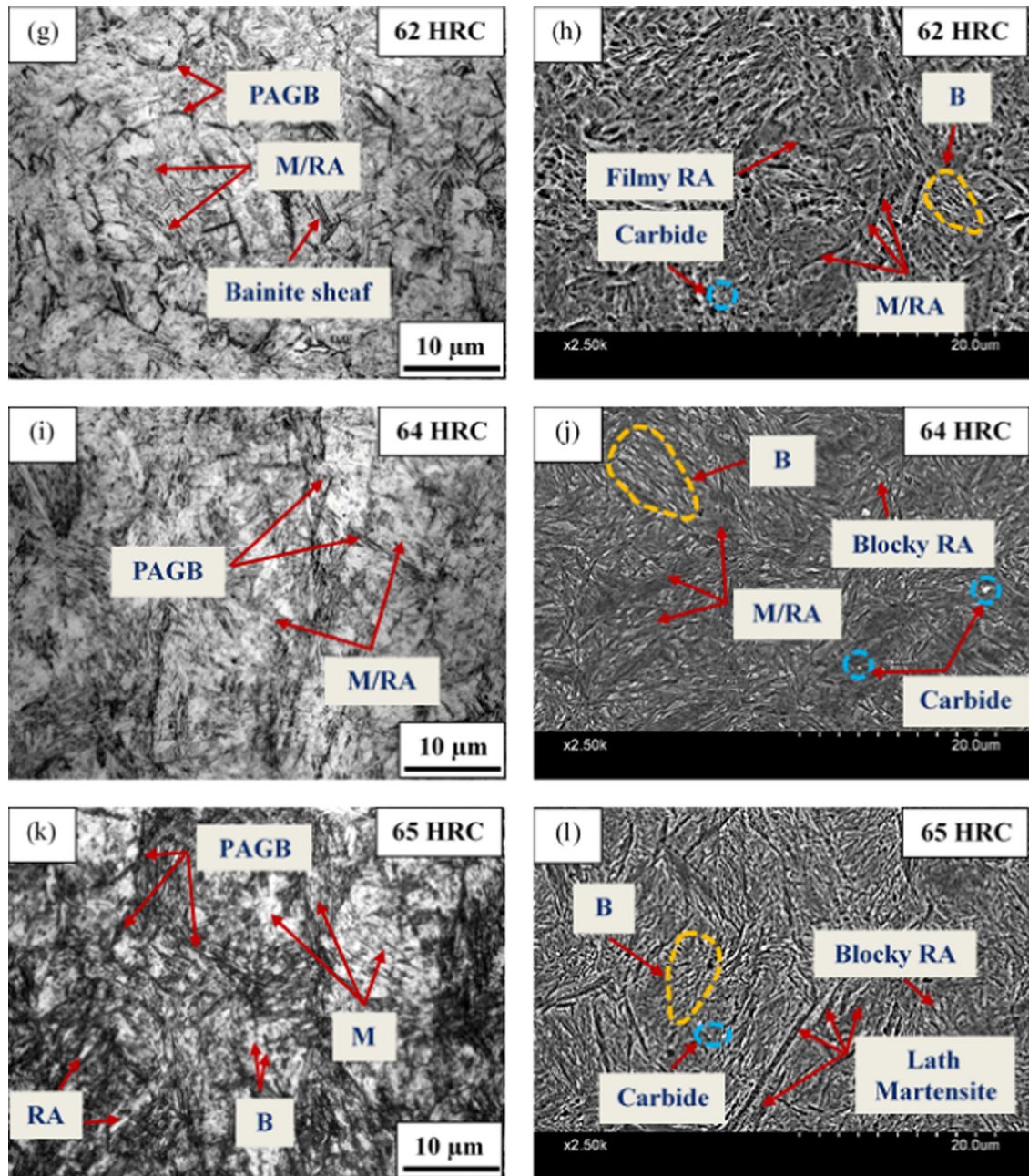


Fig. 4—continued.

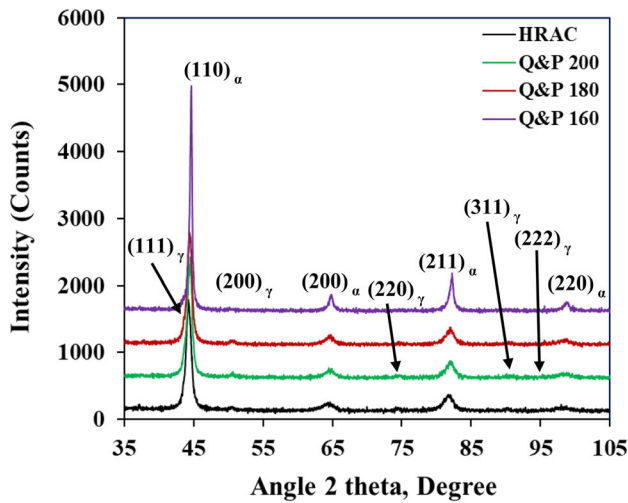
be estimated from Eqs. (12) and (13), respectively.^[42] Conversely, the formation of P in the HRAC sample agrees with the CCT curves estimated by JMatPro[®] and dilatometry results as presented in Figures 2(a) and 3(g), respectively. It is also factual that Nb retards the recrystallization kinetics by the formation of Nb (C, N) precipitates. These precipitates are beneficial for refining austenite grain size (AGS) through precipitation pinning or the solute drag effect.^[39]

$$S_v = 2/D_\gamma \quad [12]$$

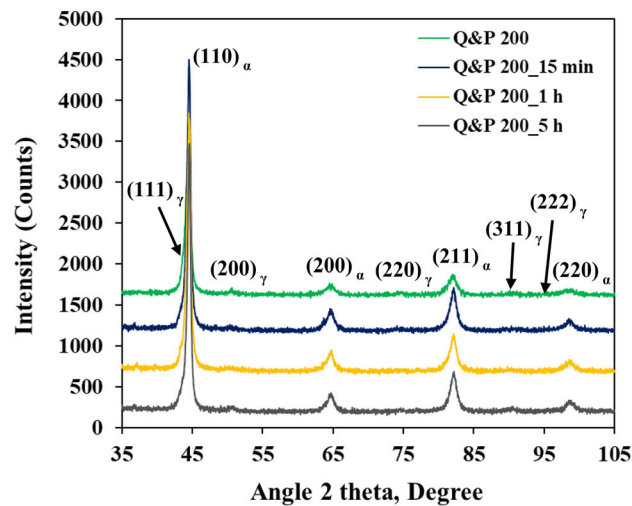
$$S_v = (1 + R + R^{-1})/D_\gamma + 0.63(100R - 30). \quad [13]$$

Here, D_γ is γ grain size (μm), and R is the average aspect ratio of the deformed γ grains.

Figures 6(c) through (g) display OM and SEM micrographs of isothermally heat-treated (IHT) samples subjected to Q&P at 200 °C, 180 °C, and 160 °C (below M_s) for 30 minutes. Q&P at 200 °C results in a mixed-phase microstructure of preformed or tempered martensite (PTM), high-carbon fresh martensite (FM) (untempered), retained austenite (RA), and some fine



(a)



(b)

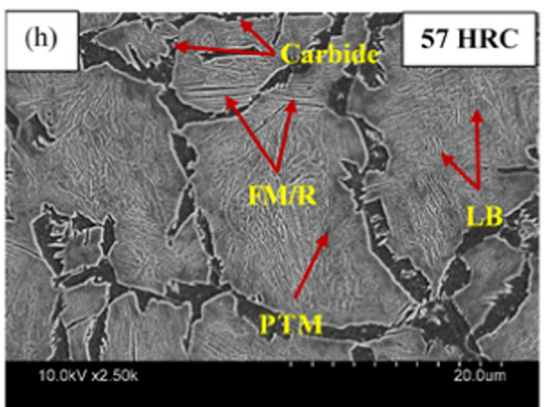
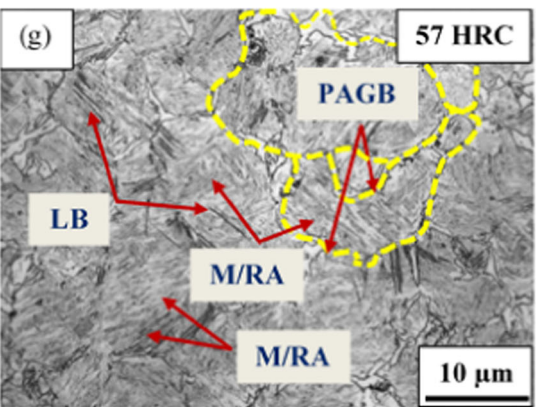
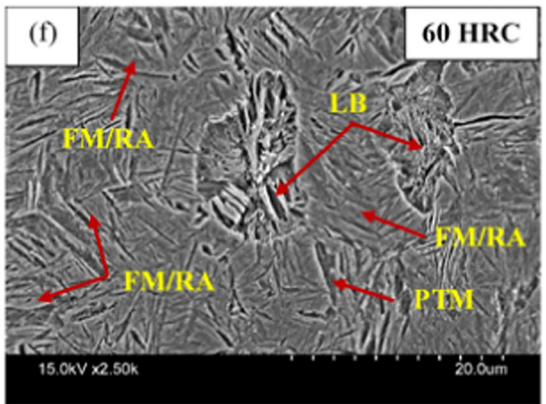
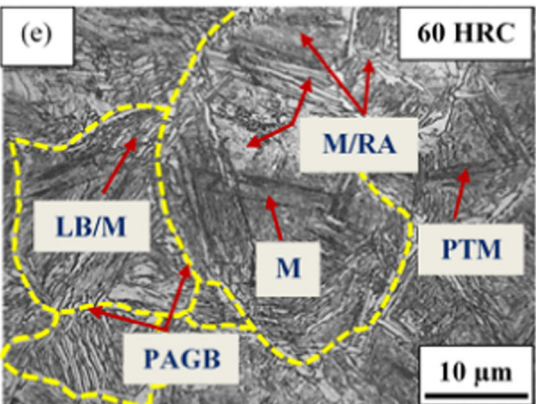
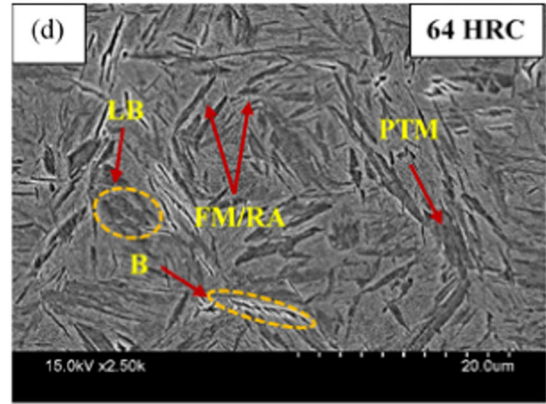
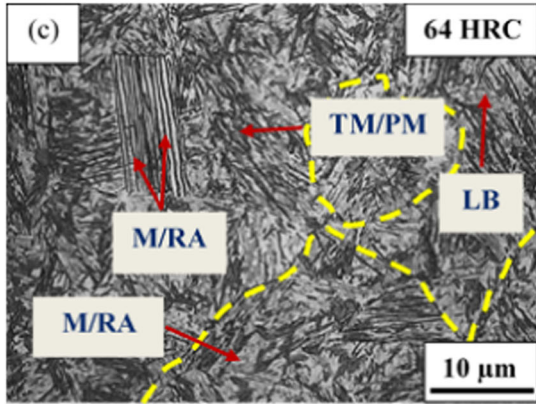
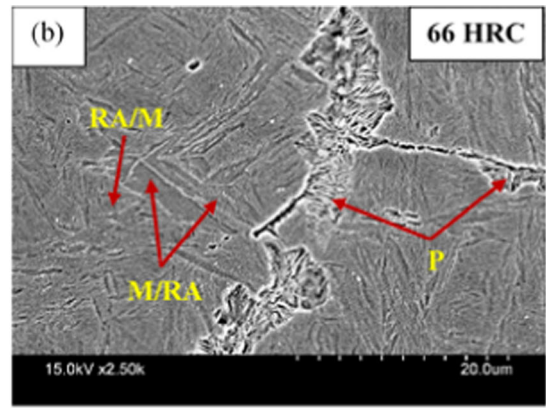
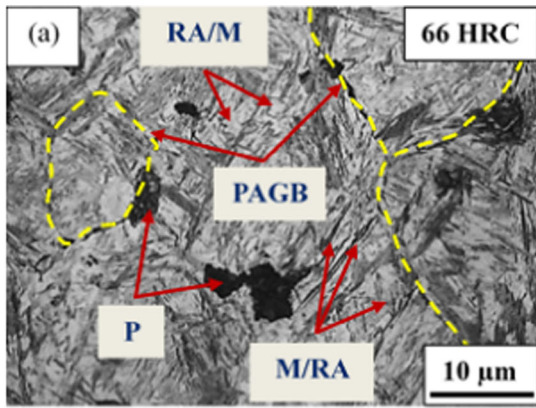
Fig. 5—X-ray diffraction patterns of hot rolled air-cooled and heat-treated samples (a) at different temperatures and (b) for different time durations.

Table IV. Calculated Volume Percentage of RA (V_r) and Carbon Concentrations in RA (C_r) Under Different Processing Conditions

Sample ID	T_p (°C)	P_t (min)	V_r (pct)	C_r (pct)
HRAC	—	—	6 ± 2	0.84
Q&P 200	200	30	10 ± 2	1.02
Q&P 180	180	30	8 ± 2	0.95
Q&P 160	160	30	< 1.5	0.56
Q&P 200_15 min	200	15	6 ± 2	0.87
Q&P 200_1 h	200	60	5 ± 2	0.82
Q&P 200_5 h	200	300	< 2	0.66

laths of lower bainite (LB) as indicated by arrows in Figures 6(c) and 6(d). Figures 6(e) and (f) display OM and SEM micrographs, respectively, of the Q&P 180 °C sample that reveal similar microstructural constituents (PTM, FM, RA, LB) as seen in Figures 6(c) and (d).

Figures 6(g) and (h) show the optical and SEM microstructures, respectively, of Q&P 160 °C samples that reveal mixed phases consisting of PTM, FM, RA, LB (like Q&P at 200 °C and 180 °C samples) with some amount of additional ferrite (F). PAGBs in the optical micrographs of Figure 6 are delineated by yellow dotted lines. The corresponding HRC values are given at the inset of each micrograph, which exhibits the increase of Q&P temperature from 160 °C to 200 °C resulting in improved hardness (≈ 7 HRC) values, which is an indication of the formation of comparatively finer secondary transformation products in higher volume percentage at comparatively higher Q&P temperature just below M_s . The stabilization of RA through C partitioning from supersaturated martensite is important since, during strain-induced transformations, it increases the ability of work-hardening of the material and thereby eliminates the problem of inferior ductility associated with fine-grained metals.^[43,44] It is noticeable that despite selecting Q&P treatment temperatures (200 °C, 180 °C, 160 °C) below $M_s \approx 217$ °C, bainite is present in all the micrographs from Figures 6(c) through (h). Bainite formation below M_s has already been witnessed by several researchers, which correlates well with the formation of ultrafine bainite and fine interlath RA.^[12,43–48] Bhadeshia has shown the relationship of M_s and B_s with C concentration (0.2 to 1.4 wt pct) in a Fe-3Mn-2Si-C steel and concluded that B_s has no specific lower limit.^[43] Conversely, the rate of bainite formation decelerates noticeably with decreasing transformation temperature.^[43] It has been reported elsewhere that the occurrence of LB is associated with the formation of lath of plate type F in the matrix, including a few C particles inclined at an angle of $\approx 60^\circ$ toward the bainitic–ferrite axis.^[49] L. Quain has reported that both FM and RA originate from the remaining untransformed austenite that could not transform to bainite after IH but transforms partially to FM during cooling to RT due to its low thermal stability.^[48] On the other hand, PTM results from supercooled austenite during cooling from the austenite region and subsequently, it is tempered during IH below M_s .^[48] The primary difference in the morphology of LB and PTM is that LB contains a specific crystallographic orientation of the carbide precipitates, whereas PTM comprises multivariant carbide precipitates.^[49] However, it is noteworthy that the chosen IH time of 30 minutes was adequate for C partitioning from supersaturated M to carbon depleted γ , which ensures suitable volume fractions of γ at room temperature and significantly reduces the possibilities of the higher amount of LB formation from unstable γ as evident here in Figures 6(c) through (h).^[49] Significant amounts of carbide precipitates and/or grain boundary ferrite (GBF) are also present in Figure 6(h), which may be formed during air cooling from 900 °C to 160 °C before Q&P because of insufficient carbon partitioning to stabilize significant RA at RT at such low temperature and due to the possibilities of formations of NbC precipitates that promotes the GBF nucleation. The high Si content in the current steel also reduces the chances of cementite formation. Yet, a TEM study is required to validate these facts further.



◀ Fig. 6—Optical and SEM micrographs of (a) & (b) hot rolled air cooled (HRAC) (FRT≈1000 °C); hot rolled air cooled followed by isothermally heat treated for 30 min (c) & (d) Q&P at 200 °C (e) & (f) Q&P at 180 °C and (g) & (h) Q&P at 160 °C samples, respectively. PAGB, P, M, RA, LB, FM, PTM, and F are the abbreviations of prior austenite grain boundary, pearlite, martensite, retained austenite, lower bainite, fresh martensite, preformed/tempered martensite, and ferrite, respectively.

Figure 7 displays the estimated volume percentage of different phases after Q&P treatment at various temperatures. The formula predicted results match well with earlier observations.^[45,48,50] The values of V_γ are taken from Table IV and the volume percentage of ferrite present in the Q&P 160 sample was predicted using ImageJ analysis software from at least 10-15 high-resolution SEM micrographs. Empirical Equations involving the calculation of respective volume percentages of final phases (PTM, FM, RA, LB) are well documented in the literature and given here in Eqs. (14) to (16).^[48]

$$V_{PTM} = 1 - e^{-1.1 \times 10^{-2} (M_s - QT)} \quad [14]$$

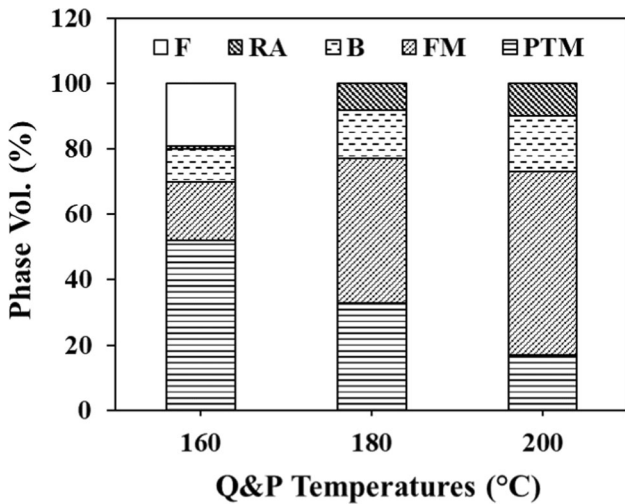


Fig. 7—Volume percentage of various constituting phases of the samples subjected to Q&P treatment at different temperatures.

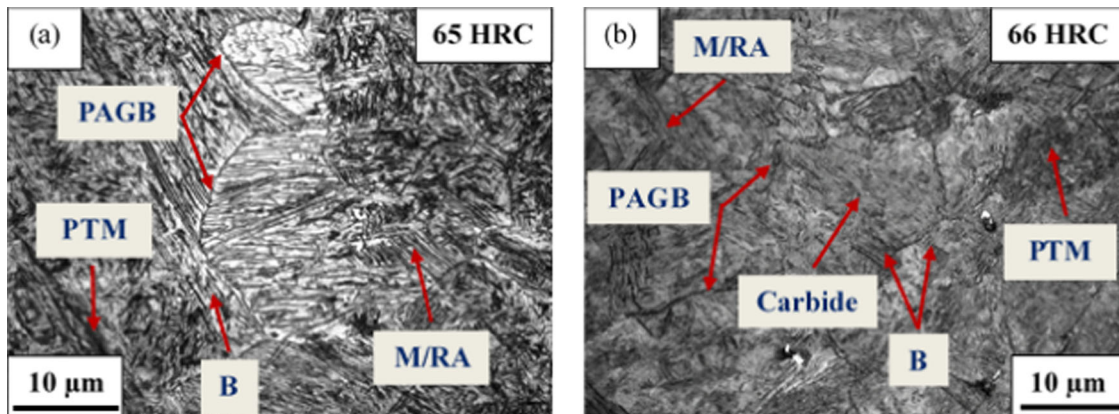


Fig. 8—Optical and SEM micrographs of (a) Q&P 200°C_15 min and (b) Q&P 200°C_5 h samples, respectively.

$$V_{FM} = \frac{V_\gamma \times (1 - e^{-1.1 \times 10^{-2} (M_s(F) - RT)})}{e^{-1.1 \times 10^{-2} (M_s(F) - RT)}} \quad [15]$$

$$V_B = (1 - V_{PTM} - V_{FM} - V_\gamma). \quad [16]$$

Here, V_{PTM} , V_γ , V_{FM} , and V_B are volume fractions of PTM, RA, FM, and LB, respectively. M_s , $M_s(F)$, QT , and RT are theoretical martensite start temperature depending on the composition, fresh martensite start temperatures, quenching, and room temperatures, respectively.

Figures 8(a) and (b) show optical micrographs of Q&P 200°C_15 min and Q&P 200°C_5 h samples, respectively. Both the microstructures mainly reveal mixed phases comprising PM, FM, B, and RA. Tempering of athermal PM and formation of B increase with increasing IH time from 15 minutes to 5 hours, as evident in Figures 6(c), (d) vis-à-vis 8(a), (b), and these findings correlate well with earlier studies.^[12,50,51] However, the slight increase of HRC values (≈2 HRC) with increasing IH time from 1 to 5 h indicates carbide precipitation, which further facilitates the decomposition of unstable γ to B. Despite the high Si content and low Q&P temperature, there may exist a strong driving force for carbide precipitations due to higher carbon content in the steel.^[12,51]

3. TEM study

Figure 9 reveals TEM micrographs of (a) HRAC with FRT 1000 °C, (c) & (d) Q&P 200 °C, (e) & (f) Q&P 180 °C, and (g) to (i) Q&P 160 °C samples. Figures 9(b) and (j) show the EDS spectrum of NbC precipitates in HRAC and Q&P 160 °C samples, respectively. Figures 9(a), (c), (e), (f), and (g) primarily show lath M structures with fine interlath RA in between them. It is visible from Figure 9 that the average lath thickness of M and RA is ~ 0.1 to 0.5 μm and 12 to 70 nm, respectively, whereas the size of B lath approached ~ 0.6 to 1 μm . RA is the dark regions present at the interlath boundaries, as evident in the bright-field (BF) images of Figures 9(a), (c), (e), and (g) and is confirmed by the bright regions in the corresponding dark-field

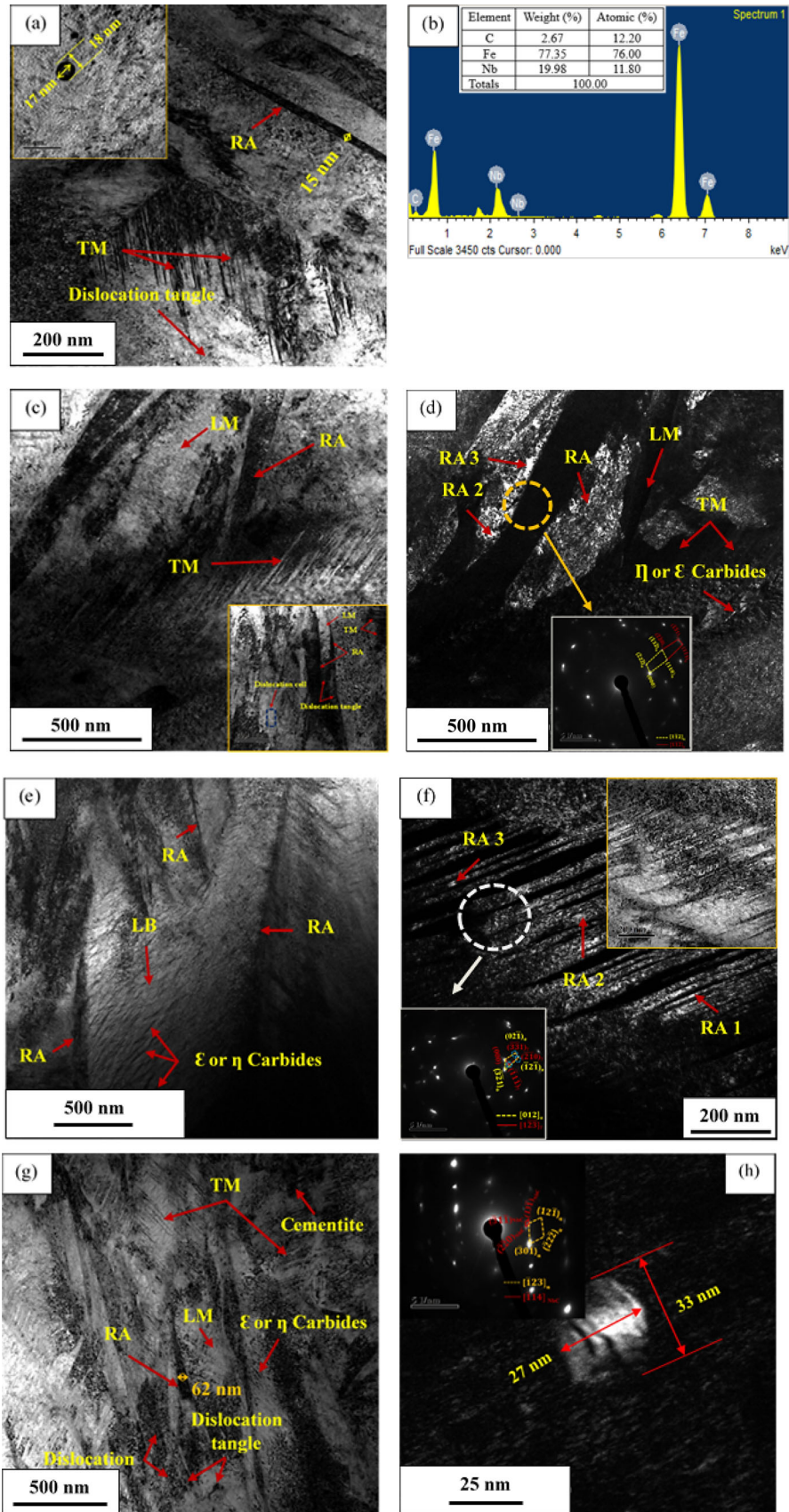


Fig. 9—TEM micrograph of (a) HRAC (FRT ≈ 1000 °C) and HRAC followed by Q&P for 30 min at (c) & (d) 200 °C, (e) & (f) 180 °C (g) to (i) 160 °C samples. (b) and (f) show the EDS spectrum of NbC precipitates.

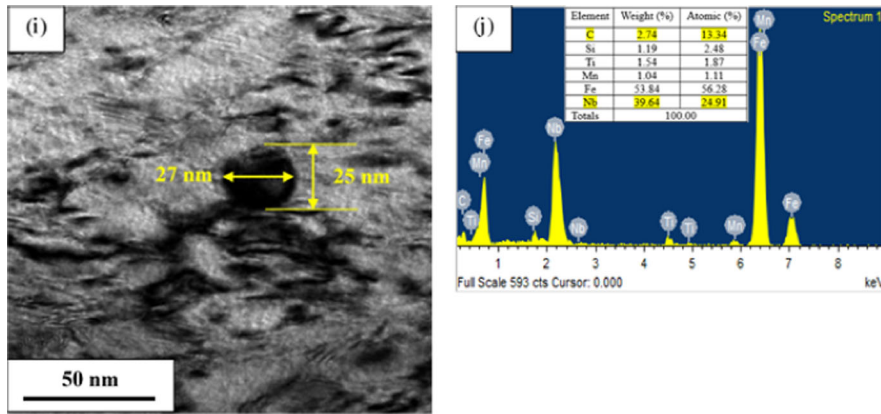


Fig. 9—continued.

Table V. Values of A and B for the Determination of k_s

Formula	A	B
Irvine <i>et al.</i>	6770	2.26
Narita <i>et al.</i>	7900	3.42

(DF) images [Figures 9(d) and (f)]. It is noticeable from Figures 9(d) and (f) that three different morphologies of RA, *i.e.*, film, blocky, and chunk types denoted as RA 1, RA 2, and RA 3, respectively, are present in the DF microstructures that result from different C partitioning mechanisms from the matrix.^[52–54] It is noticeable from Figure 9 that parallel M variants exhibit different bright and dark contrast blocks. The black-dotted structures in dark M blocks are reported as high-density dislocations in TM and untwinned M.^[11,55] C depleted M lath with dislocation tangle (marked in red arrows) represents a high density of dislocation as evident in the inset of Figures 9(a), (c), and (g). A dislocation cell is also found with dislocation density comparatively higher in the wall and lower at the center, as indicated by the arrow at the inset of Figure 9(c). The DF images of the selected diffraction spots of the SAED pattern corresponding to FCC RA at the inset of Figures 9(d) and (f) confirm the presence of interlath austenite films in between the martensite laths which follow $(1\bar{1}2)_\alpha // (1\bar{1}2)_\gamma$ (closely related to K–S orientation relationship) and $(012)_\alpha // (1\bar{2}3)_\gamma$ orientation relationships. C-enriched secondary twin martensite is also observed [denoted by arrows in Figures 9(a), (c), and (g)] in HRAC and Q&P samples that is expected to form at the final stages of cooling to room temperature from carbon-enriched austenite. It has already been reported that the formation of twins in high-carbon steels occurs due to the accommodation of the transformation strains during M transformation.^[11,55,56] The existence of LB is confirmed in Figure 9(e), where carbides with thickness < 10 nm are dispersed at an angle of $\approx 55^\circ$ to the longitudinal lath axis of LB. It is visible from Figures 9(c) through (f) vis-à-vis Figure 9(g) that with decreasing partitioning temperatures, the stabilization of austenite becomes less

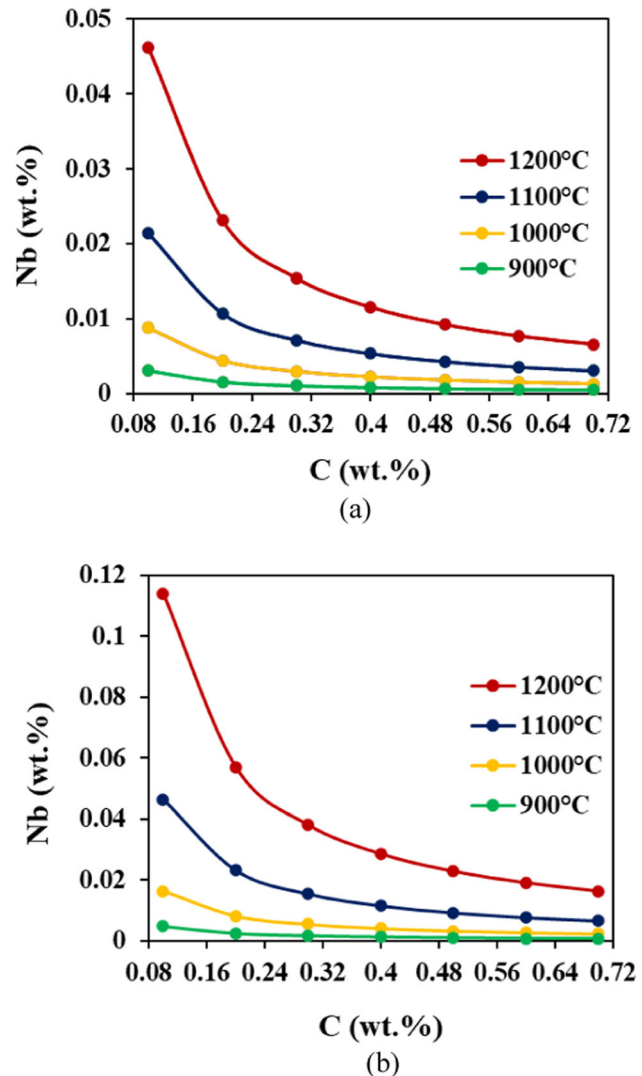


Fig. 10—Solubility product of NbC at different temperatures calculated using (a) Irvine and (b) Narita's Equations.

effective, whereas precipitation of transition carbides (η/ϵ) increases remarkably.^[3,5,55–58] It is predictable that these transitional carbides that are visible at

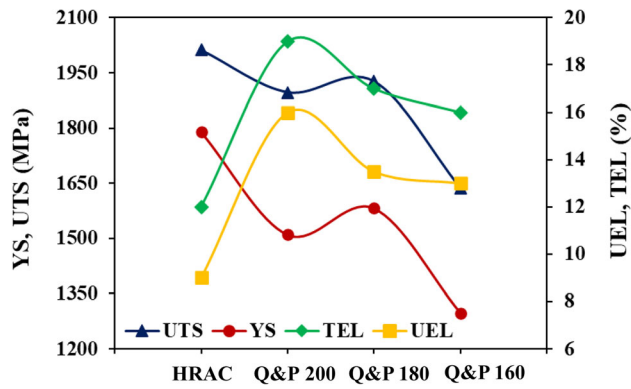


Fig. 11—Tensile test results of HRAC and HRAC followed by Q&P samples.

comparatively low partitioning temperatures could plausibly be dissolved at higher temperatures and can be considered as an effective source of C, either for the equilibrium Fe_3C formation or for the enrichment of untransformed γ .^[59] It has been reported earlier that although the SAED pattern of both ϵ and η carbides are almost similar, the main difference lies in their crystal structure, which is hexagonal for the prior and orthorhombic for the later one.^[11] It is pertinent that in some areas of Q&P 160 °C, small evidence of cementite precipitation at the inter and intralath positions is witnessed from the respective BF image in Figures 9(g), which correlates well with the SEM microstructures in Figures 6(h). A similar study by I. Miettunen *et al.* reported the presence of fine η carbides and large cementite precipitates in the M laths with Si content of 1.51 and 0.25 wt pct, respectively, for 0.4C steel.^[11] It is notable that the heterogeneous distribution of η/ϵ carbides within the martensite laths is attributed to the fact that the possibilities of carbon escaping to the interlath RA regimes prior to precipitation enhance with the refinement of crystal size. In another way, the absence of interlath RA film might be another reason for carbide precipitation due to the unavailability of the immediate adjacent sinks for the C atoms.^[11] Therefore, from the above discussion, it can be stated that significant suppression of cementite formation at comparatively higher temperatures and marginal suppression of transition carbide formations at lower temperatures was noticed due to the presence of the adequate amount of Si in the present steel, which is the main difference in partitioning nature under three different Q&P conditions.^[5,57,58]

A very fine NbC precipitate (≈ 18 nm) is shown in the inset of Figure 9(a) found in the HRAC sample. The corresponding EDS spectrum in Figure 9(b) indicates NbC precipitate formation. Additionally, two other fine NbC precipitates (≈ 27 nm) are also observed in Q&P 160 °C samples, as shown by the DF and BF images in Figures 9(h) and (i), respectively. The corresponding SAED analysis at the inset of Figure 9(h) reveals that it follows $(\bar{1}23)_\alpha // (\bar{1}14)_{\text{NbC}}$ orientation relationship with M matrix. The corresponding EDS spectrum in Figure 9(j) indicates the presence of these NbC

precipitates. The solubility product of NbC at different temperatures can be calculated from Eqs. (17) to (20).^[57,60]

$$k_s = a_M a_X / a_{MX} \quad [17]$$

$$k_s = \frac{f_M [M] \cdot f_X [X]}{a_{MX}} \quad [18]$$

$$k_s = [M] \cdot [X] \quad [19]$$

$$\log_{10} k_s = B - \left(\frac{A}{T} \right), \quad [20]$$

where a_M and a_X are activities of microalloying (Nb) and interstitial elements in solutions, respectively, in equilibrium with compound MX; a_{MX} is the activity of the reaction product or constituent phase; f_M and f_X are activity coefficients of Nb and C, respectively; $[M]$ and $[X]$ are solute concentrations; T is the thermodynamic temperature (K); B and A are constants and values of which are given in Table V.

Figures 10(a) and (b) represent the solubility product of NbC at different temperatures estimated by using Irvine and Narita's Equations, respectively.^[60] Speer *et al.* have reported that at 1250 °C, the solubility of Nb in γ is < 0.04 wt pct and < 0.02 wt pct at a C level of 0.02 wt pct and 0.4 wt pct, respectively, which agrees well with the plots in Figure 10(a) and shows slight deviations from the results shown in Figure 10(b).^[61] It can be seen from Figure 10(a) that < 0.01 wt pct and < 0.005 wt pct Nb is soluble in γ at 1200 °C and 1100 °C, respectively, while these values are ≈ 0.02 wt pct and ≈ 0.01 wt pct in Figure 10(b) with the present C content (0.68 wt pct) in the steel. It is visible from Figures 10(a) and (b) that the solubility of Nb in γ is very low at or below 1000 °C. It is also factual that Irvine's Equation reflects a complex niobium carbonitride, whereas Narita's Equation relates specifically to NbC.^[60] In this context, the relative atomic masses of Nb and C are 93 and 12, respectively, which indicates that at a 1:1 ratio of Nb and C on a molar basis, the stoichiometric line has a steep slope and will coincide with Y-axis, which directs that for NbC precipitation, only a small fraction of the total C is required for the present composition. Hence, it can be concluded that most of the remaining C has significantly contributed to the partitioning process, thereby resulting in γ stabilization.

The correlation of $[M] \cdot [X]$ with T in Eq. [20] indicates the monotonic increase of NbC content with the decrease of temperature, which includes the nucleation and growth of coherent NbC precipitate within γ or M.^[62] Quite finer NbC precipitates (≈ 9 nm) are witnessed in HRAC samples [Figures 9(a) and (b)] than the Q&P160 samples. It is apparent from Figures 6(a) and (b) that some amount of P is present in the HRAC

Table VI. Summarized Outcomes After Q&P Treatment from the Present Study and Published Literature

Sl. No.	Steel Composition (wt pct)	Phase Constituents	Mechanical Properties		Major Findings	References
			Hardness (HRC*)	Product of UTS and TEL (MPa pct)		
1.	Fe-0.554C-1.72Si-0.851Mn-0.149Cr	M + RA	46	—	higher γ stabilization at lower QT. higher Si facilitates transition carbide at a lower temperature.	4
2.	Fe-1.01C-2.03Si-0.356Mn-1.45Cr	M + RA + cementite	44	—	high Cr leads to large Fe ₃ C formation during spheroidizing, thereby leading to inadequate C partitioning.	4
3.	Fe-0.4C-1.51Si-2.05Mn-0.02Al-1Cr-0.49Ni	M + RA	—	—	low Si exhibited substantial B formation, and \approx 4 pct RA was stabilized at RT during partitioning at 300 °C even after 1000 s, whereas high Si enabled retention of γ (\approx 18 pct) under similar conditions.	11
4.	Fe-0.529C-1.670Si-0.720Mn-0.120Cr	M + RA + B + carbide	58	—	\approx 18 pct RA obtained at RT; \approx 5 pct RA stabilized after IH	12
5.	Fe-0.28C-0.66Si-1.46Mn-0.18Cr-0.11V	M + RA	—	24672	at 200 °C for only 5 s. \approx 4.5 to 6.3 pct RA was stabilized in the microstructure.	65
6.	Fe-0.63C-1.52Mn-1.49Si-0.62Cr-0.036Nb	M + RA	—	24180	Q-P-T process results in 29.1 pct RA, while traditional Q&T process leads to only 7.1 pct RA.	64
7.	Fe-0.68C-1.72Mn-2.2Si-0.036Nb	M + RA + B	66	36043	\approx 10 pct RA stabilized at RT and Si effectively inhibits carbide formations despite high C. Very fine NbC precipitates are observed in a few samples.	Current paper

*Maximum HV values are converted to HRC values.

sample. Hence, during air cooling from 900°C to 160°C there are possibilities of ferrite formation at the grain boundaries because of two reasons. Firstly, insufficient C partitioning from M to γ despite 30 minutes of holding at such low partitioning temperature and the presence of high Si as an inhibitor to cementite formation leaves only the options of F nucleation at the grain boundaries [Figures 6(g) and (h)]. Secondly, the preformed NbC precipitates can provide a surface for F nucleation and growth. Moreover, less RA in the Q&P 160 sample [Figure 5(a)] because of the low degree of C enrichment to γ indicates the possibilities of NbC precipitation due to the strong affinity of Nb to C. It might be true that some fine NbC precipitates are also present in Q&P 180 and Q&P 200 samples; however, they are not detected in TEM. It is also notable that the precipitation of NbC in both these samples is not witnessed due to effective C partitioning from supersaturated M to γ and, thereby, reducing the available C content to combine with Nb to form NbC precipitates. Hence, it can be said that the decrease in RA in the Q&P 160 sample is caused by the increase in precipitate density and growth of existing precipitates by the consumption of carbon in γ .^[63] In an earlier study, precipitation of NbC was also found in a Fe-0.63C-1.52Mn-1.49Si-0.62Cr-0.036Nb steel subjected to quenching at 160 °C followed by partitioning and tempering at 400 °C for 60 seconds.^[64]

4. Tensile testing

Figure 11 displays tensile test results of hot rolled air cooled (FRT \approx 1000 °C); hot rolled air cooled followed by heat treated (quenching and partitioning at 200 °C, 180 °C, and 160 °C) samples. For the Q&P 180 sample, the significant increase in yield strength (YS) (\approx 72 MPa) and marginal rise in ultimate tensile strength (UTS) (\approx 30 MPa) as compared to the Q&P 200 sample are attributed to increasing M content, as evident in Figure 7 and decreasing trend of strain hardening ability. The latter one is mainly associated with less RA content, as apparent from Figure 5(a). It cannot be overruled that the strength effect of LB can compensate for the declining UTS values to a certain extent, which is associated with decreasing M content.^[49] However, the highest YS and UTS values \approx 1790 MPa and \approx 2010 MPa, respectively, in the HRAC sample are associated with carbon-enriched M formation due to direct cooling after HR in combination with the formation of fine NbC precipitates [Figure 9(a)] that significantly contributes to the refinement of lower temperature transformation products and in precipitation strengthening. The lowest values of YS (\approx 1298 MPa) and UTS (\approx 1637 MPa) are observed in the Q&P 160 sample which may be due to the formation of softer phases like ferrite (\approx 15 vol. pct) in this steel [Figures 6(h) and 7] although there also exists the possibilities of significant precipitation strengthening due to the formation of fine NbC precipitates as evident in Figures 9(h) through (j). The highest total elongation (TEL) is observed in the Q&P 200 sample (\approx 19 pct) followed by Q&P 180 (\approx 17 pct), Q&P 160 (\approx 16 pct) and HRAC (\approx 12 pct) sample which mainly attributed to the

difference in phase constituents (RA and F) as discussed above and the C content in RA that determines its stability at RT as shown in Table IV. During tensile testing, RA yields first with the increasing load and eventually, it transfers part of the load to B and M when the load is significantly higher.^[54] It is also factual that the various types of RA have different morphologies and volume fractions with different mechanical stability.^[54] It has been reported earlier that the C content in coarse blocky RA is comparatively less than fine interlath RA films, which leads to instability of the blocky RA at RT.^[49] Table VI summarizes the outcomes obtained after Q&P treatment from the present study and published literature. Therefore, from the present study, it can be concluded that the best combinations of strength and ductility in Q&P 200 samples (36043 MPa pct) followed by Q&P 180 samples (32759 MPa pct) in the present study are attributed to the transformation-induced plasticity (TRIP) effect of different RA that plays significant roles on stress relief, suppression of the microcrack formations, and hindering the propagations of the microcracks at higher strains by increasing the total path length of the microcracks.^[49,54]

IV. CONCLUSIONS

The significant conclusions obtained from the present study can be summarized as follows:

1. Increasing the cooling rate (CR) to a certain degree initially suppresses the transformation temperatures and leads to the formation of lower temperature transformation products. The observation has been endorsed during the enhancement of CR from 0.5 to 5 °C/s, which lowers the P_s , P_f , B_s , and B_f temperatures to the tune of \sim 70 °C, \sim 73 °C, \sim 12 °C, and \sim 8 °C, respectively. However, further increase of CR from 5 to 50 °C/s results in the suppression in B_s and B_f temperatures to the extent of \sim 17 °C and \sim 20 °C, respectively, and increase in M_s temperature from 217 °C to 253 °C.
2. Q&P near the M_s temperature results in the highest volume fraction of RA at room temperature. The highest values of V_γ and C_γ have been obtained in Q&P 200 sample followed by Q&P 180, Q&P 200_15 min, HRAC, and Q&P 200_1 h samples, respectively. The highest values of V_γ and C_γ in Q&P 200 sample are associated with sufficient C partitioning from supersaturated M to carbon depleted γ at 200°C which is just below the M_s , whereas the lowest values of V_γ and C_γ are obtained for Q&P 160 and Q&P 200_5 h samples.
3. HRAC sample reveals microstructures comprising M, P, and interlath RA films. In contrast, Q&P 200 and Q&P 180 samples show mixed-phase microstructures consisting of PTM, high-carbon FM, RA (films and blocky shapes), and some LB. The average lath thickness of M and RA is \approx 0.1 to 0.5 μ m and 12 to 70 nm, respectively. For B, it is found to be \approx 0.6-1 μ m. Q&P 160 sample reveals

mixed phases consisting of PTM, FM, RA, and LB with some amount of F.

4. Tempering of athermal M and formation of B increase with increasing IH time from 15 minutes to 5 hours at 200°C. The formation of C-enriched TM is evident in TEM observations for both HRAC and Q&P samples.
5. The hardness values increase significantly (≈ 32 HRC) with the increasing CRs from 0.5 to 50 °C/s. The higher HRC values in the Q&P 200 sample than that of the Q&P 180 and Q&P 160 samples are attributed to more C-enriched FM formation while cooling from Q&P temperature to RT and significant ferrite formation, respectively.
6. The formation of hard phase like fresh martensite increases the strength. At the same time, the presence of RA increases the ductility without compromising the strength. The highest YS and UTS values ≈ 1790 MPa and ≈ 2010 MPa, respectively, are observed in the HRAC sample. The lowest values of YS (≈ 1298 MPa) and UTS (≈ 1637 MPa) are observed in the Q&P 160 sample. However, the best combination of strength and ductility is witnessed in Q&P 200 samples (≈ 36043 MPa pct) followed by Q&P 180 samples (≈ 32759 MPa pct).

DATA AVAILABILITY

Data will be made available on request.

CONFLICT OF INTEREST

The authors declare no conflict of interest.

REFERENCES

1. R.K. Barik, A. Ghosh, M.B. Sk, S. Biswal, A. Dutta, and D. Chakrabarti: *Acta Mater.*, 2021, vol. 214, 116988. <https://doi.org/10.1016/j.actamat.2021.116988>.
2. S. Behera, R.K. Barik, M.B. Sk., R. Mitra and D. Chakrabarti: *Mater. Sci. Eng. A*, 2019, vol. 764, 138256. <https://doi.org/10.1016/j.msea.2019.138256>.
3. J. Kobayashi, S.M. Song, and K. Sugimoto: *ISIJ Int.*, 2012, vol. 52(6), pp. 1124–29. <https://doi.org/10.2355/isijinternational.52.1124>.
4. S.S. Nayak, R. Anumolu, R.D.K. Misra, K.H. Kim, and D.L. Lee: *Mater. Sci. Eng. A*, 2008, vol. 498, pp. 442–56. <https://doi.org/10.1016/j.msea.2008.08.028>.
5. J.G. Speer, D.K. Matlock, B.C. De Cooman, and J.G. Schroth: *Acta Mater.*, 2003, vol. 51, pp. 2611–22. [https://doi.org/10.1016/S1359-6454\(03\)00059-4](https://doi.org/10.1016/S1359-6454(03)00059-4).
6. G. Mandal, S.K. Ghosh, S. Bera, and S. Mukherjee: *Mater. Sci. Eng. A*, 2016, vol. 676, pp. 56–64. <https://doi.org/10.1016/j.msea.2016.08.094>.
7. M.J. Santofimia, L. Zhao, R. Petrov, C. Kwakernaak, W.G. Sloof, and J. Sietsma: *Acta Mater.*, 2011, vol. 59(15), pp. 6059–68. <https://doi.org/10.1016/j.actamat.2011.06.014>.
8. M.J. Santofimia, R.H. Petrov, L. Zhao, and J. Sietsma: *Mater. Char.*, 2014, vol. 92, pp. 91–95. <https://doi.org/10.1016/j.matchar.2014.03.003>.
9. F. Hajyabary, J. Sietsma, G. Miyamoto, T. Furuhashi, and M.J. Santofimia: *Acta Mater.*, 2016, vol. 104, pp. 72–83. <https://doi.org/10.1016/j.actamat.2015.11.032>.
10. E.P. Da Silva, D. De Knijf, W. Xu, C. Fojer, Y. Houbaert, J. Sietsma, and R. Petrov: *Mater. Sci. Technol.*, 2015, vol. 31, pp. 808–16. <https://doi.org/10.1179/1743284714y.0000000719>.
11. I. Miettunen, S. Ghosh, M.C. Somani, S. Pallaspuuro, and J. Komi: *J. Mater. Res. Technol.*, 2021, vol. 11, pp. 1045–60. <https://doi.org/10.1016/j.jmrt.2021.01.085>.
12. S. Pashangeh, M.C. Somani, S.S.G. Banadkouki, H.R.K. Zarchi, P. Kaikkonen, and D.A. Porter: *Mater. Charact.*, 2020, vol. 162, p. 110224. <https://doi.org/10.1016/j.matchar.2020.110224>.
13. D.T. Pierce, D.R. Coughlin, D.L. Williamson, K.D. Clarke, A.J. Clarke, J.G. Speer, and E. De Moor: *Acta Mater.*, 2015, vol. 90, pp. 417–30. <https://doi.org/10.1016/j.actamat.2015.01.024>.
14. B. Kim, J. Sietsma, and M.J. Santofimia: *Mater. Des.*, 2017, vol. 127, pp. 336–45. <https://doi.org/10.1016/j.matdes.2017.04.080>.
15. A.L.A. de Araujo: *Mines Theses & Dissertations*, 2016, pp. 1–118. <https://hdl.handle.net/11124/170039>.
16. Q. Feng, L. Li, W. Yang, and Z. Sun: *Mater. Sci. Eng. A*, 2014, vol. 605, pp. 14–21. <https://doi.org/10.1016/j.msea.2014.03.051>.
17. E. Pereloma, I. Timokhina, and P. Hodgson: *Mater. Sci. Eng. A*, 1999, vol. 273–275, pp. 448–52.
18. J. Zhang, Z. Dai, L. Zeng, X. Zuo, J. Wan, Y. Rong, N. Chen, J. Lu, and H. Chen: *Acta Mater.*, 2021, vol. 217, p. 117176. <https://doi.org/10.1016/j.actamat.2021.117176>.
19. I. Dey, R. Saha, and S.K. Ghosh: *Int. J. Mater. Product Technol.*, 2021, vol. 62(1/2/3), pp. 111–25. <https://doi.org/10.1504/IJMPT.2021.115216>.
20. N. Zhong, X.D. Wang, L. Wang, and Y.H. Rong: *Mater. Sci. Eng. A*, 2009, vol. 506, pp. 111–16. <https://doi.org/10.1016/j.msea.2008.11.014>.
21. J. Trzaska, A. Jagiello, and L.A. Dobrzanski: *Arch. Mater. Sci. Eng.*, 2009, vol. 39, pp. 13–20.
22. M. Avrami: *J. Chem. Phys.*, 1940, vol. 8, pp. 212–24. <https://doi.org/10.1063/1.1750631>.
23. J. Johnson and R. Mehl: *Trans. AIMME*, 1939, vol. 135, pp. 416–58.
24. E. Scheil: *Archiv Eisenhüttenwes*, 1935, vol. 8, pp. 565–67. <https://doi.org/10.1002/srin.193500186>.
25. J.S. Kirkaldy, B.A. Thomson, and E.A. Baganis: eds. J. S. Kirkaldy and D. V. Doane, (Warrendale, PA: AIME), 1978, 82.
26. N. Saunders, Z. Guo, X. Li, A.P. Miodownik, and J.P. Schille: *JMatPro Software Literature*, 2004, pp. 1–12.
27. M.V. Li, D.V. Niebuhr, L.L. Meekisho, and D.G. Atteridge: *Metall. Mater. Trans. B*, 1998, vol. 29B, pp. 661–72.
28. A.A. Gorni: *Steel forming and heat-treating Handbook*, 2014, pp. 1–46.
29. H.S. Yang and H.K.D.H. Bhadeshia: *Scr. Mater.*, 2009, vol. 60, pp. 493–95. <https://doi.org/10.1016/j.scriptamat.2008.11.043>.
30. P. Schulze, E. Schmidl, and T. Lampke: *WOMag*, 2014, vol. 3.
31. B.A. Behrens, A. Chugreev, and C. Kock: *5th Int. Conf., IOP Conf. Series: Mater. Sci. Eng.*, 2019, vol. 461, 012040. <https://doi.org/10.1088/1757-899X/461/1/012040>.
32. F. Nurnberger, O. Grydin, M. Schaper, F.W. Bach, B. Koczurkiewicz, and A. Milenin: *Steel Res. Int.*, 2010, vol. 81(3), pp. 224–33. <https://doi.org/10.1002/srin.200900132>.
33. N. Isasti, D.J. Badiola, M.L. Taheri, and P. Uranga: *Metall. Mater. Trans. A*, 2013, vol. 44A, pp. 3552–63. <https://doi.org/10.1007/s11661-013-1738-3>.
34. Z. Babasafari, A.V. Pan, F. Pahlevani, R. Hossain, V. Sahajwalla, M. Toit, and R. Dippenaar: *J. Mater. Res. Technol.*, 2020, vol. 9(6), pp. 15286–297. <https://doi.org/10.1016/j.jmrt.2020.10.071>.
35. M. Nikraves, M. Naderi, and G.H. Akbari: *Mater. Sci. Eng. A*, 2012, vol. 540, pp. 24–29. <https://doi.org/10.1016/j.msea.2012.01.018>.
36. S.S. Souza, P.S. Moreira, and G.L. Faria: *Mater. Res.*, 2020, vol. 23(1), e20190570, pp. 1–9. <https://doi.org/10.1590/1980-5373-MR-2019-0570>.
37. C.G. de Andres, F.G. Caballero, C. Capdevila, and L.F. Alvarez: *Mater. Charact.*, 2002, vol. 48, pp. 101–11. [https://doi.org/10.1016/S1044-5803\(02\)00259-0](https://doi.org/10.1016/S1044-5803(02)00259-0).
38. J.C. Zhao and M.R. Notis: *Mater. Sci. Eng. R*, 1995, vol. 15, pp. 135–208. [https://doi.org/10.1016/0927-796X\(95\)00183-2](https://doi.org/10.1016/0927-796X(95)00183-2).
39. F. Peng, Y. Xu, X. Gu, Y. Wang, X. Liu, and J. Li: *Mater. Sci. Eng. A*, 2018, vol. 723, pp. 247–58. <https://doi.org/10.1016/j.msea.2018.03.061>.

40. B.D. Cullity, and S.R. Stock: *Elements of X-ray diffraction (3rd ed.)*, 2001, pp. 363–383.
41. *Analytical methods for materials, Precise lattice parameter determination*. https://weavergroup.ua.edu/uploads/4/8/9/0/48901279/1ab3_-_precise_lattice_parameter_determination.pdf.
42. A.J. DeArdo: *Ironmak. Steelmak.*, 2001, vol. 28(2), pp. 138–44. <https://doi.org/10.1179/030192301678055>.
43. H.K.D.H. Bhadeshia: *Proc. R. Soc. A*, 2010, vol. 466, pp. 3–18. <https://doi.org/10.1098/rspa.2009.0407>.
44. H.K.D.H. Bhadeshia: *Mater. Sci. Technol.*, 1999, vol. 15, pp. 22–29. <https://doi.org/10.1179/026708399773002773>.
45. A.N. Lopez, J. Hidalgo, J. Sietsma, and M.J. Santofimia: *Mater. Sci. Eng. A*, 2018, vol. 735, pp. 343–53. <https://doi.org/10.1016/j.msea.2018.08.047>.
46. L. Zhao, L. Qian, Q. Zhou, D. Li, T. Wang, Z. Jia, F. Zhang, and J. Meng: *Mater. Des.*, 2019, vol. 183, p. 108123. <https://doi.org/10.1016/j.matdes.2019.108123>.
47. J. Tian, G. Xu, M. Zhou, and H. Hu: *Steel Res. Int.*, 2018, vol. 89, p. 1700469. <https://doi.org/10.1002/srin.201700469>.
48. L. Qian, Z. Li, T. Wang, D. Li, F. Zhang, and J. Meng: *J. Mater. Sci. Technol.*, 2022, vol. 96, pp. 69–84. <https://doi.org/10.1016/j.jmst.2021.05.002>.
49. W.S. Li, H. Gao, Z. Li, H. Nakashima, S. Hata, and W.H. Tian: *Int. J. Miner. Metall. Mat.*, 2016, vol. 23(3), pp. 303–13. <https://doi.org/10.1007/s12613-016-1239-7>.
50. A.N. Lopez, J. Hidalgo, J. Sietsma, and M.J. Santofimia: *Mater. Charact.*, 2017, vol. 128, pp. 248–56. <https://doi.org/10.1016/j.matchar.2017.04.007>.
51. S. Pashangeh, M. Somani, and S.S.G. Banadkoukia: *J. Mater. Res. Technol.*, 2020, vol. 9(3), pp. 3438–46. <https://doi.org/10.1016/j.jmrt.2020.01.081>.
52. Y.J. Li, J. Kang, W.N. Zhang, D. Liu, X.H. Wang, G. Yuan, R.D.K. Misra, and G.D. Wang: *Mater. Sci. Eng. A*, 2018, vol. 710, pp. 181–91. <https://doi.org/10.1016/j.msea.2017.10.104>.
53. Y.J. Li, D. Liu, D. Chen, J. Kang, X.H. Wang, G. Yuan, R.D.K. Misra, and G.D. Wang: *Mater. Sci. Eng. A*, 2019, vol. 753, pp. 197–207. <https://doi.org/10.1016/j.msea.2019.03.043>.
54. G. Gao, H. Zhang, Z. Tan, W. Liu, and B. Bai: *Mater. Sci. Eng. A*, 2013, vol. 559, pp. 165–69. <https://doi.org/10.1016/j.msea.2012.08.064>.
55. S. Ghosh, P. Kaikkonen, V. Javaheri, A. Kaijalainen, I. Miettinen, M. Somani, J. Komi, and S. Pallaspuuro: *J. Mater. Res. Technol.*, 2022, vol. 17, pp. 1390–407. <https://doi.org/10.1016/j.jmrt.2022.01.073>.
56. P. Zhang, Y. Chen, W. Xiao, D. Ping, and X. Zhao: *Prog. Natl. Sci.: Mater. Int.*, 2016, vol. 26, pp. 169–72. <https://doi.org/10.1016/j.pnsc.2016.03.004>.
57. J.G. Speer, D.V. Edmonds, F.C. Rizzo, and D.K. Matlock: *Curr. Opin. Solid State Mater. Sci.*, 2004, vol. 8, pp. 219–37. <https://doi.org/10.1016/j.cossms.2004.09.003>.
58. J.G. Speer, F.C.R. Assunção, D.K. Matlock, and D.V. Edmonds: *Mater. Res.*, 2005, vol. 8(4), pp. 417–23. <https://doi.org/10.1590/S1516-14392005000400010>.
59. D.V. Edmonds, K. He, F.C. Rizzo, B.C. De Cooman, D.K. Matlock, and J.G. Speer: *Mater. Sci. Eng. A*, 2006, vol. 438–440, pp. 25–34. <https://doi.org/10.1016/j.msea.2006.02.133>.
60. T. Gladman: *The Physical Metallurgy of Microalloyed Steels*, 1997, ISBN 0 910716 81 2, pp. 81–135.
61. J.G. Speer, A.L. Araujo, D.K. Matlock, and E. De Moor: *Mater. Sci. Forum*, 2016, vol. 879, pp. 1834–40. <https://doi.org/10.4028/www.scientific.net/MSF.879.1834>.
62. X.D. Wang, W.Z. Xu, Z.H. Guo, L. Wang, and Y.H. Rong: *Mater. Sci. Eng. A*, 2010, vol. 527, pp. 3373–78. <https://doi.org/10.1016/j.msea.2010.02.026>.
63. J. Zhang, H. Ding, R.D.K. Misra, and C. Wang: *Mater. Sci. Eng. A*, 2015, vol. 641, pp. 242–48. <https://doi.org/10.1016/j.msea.2015.06.050>.
64. S. Qin, Y. Liu, Q. Hao, Y. Wang, N. Chen, X. Zuo, and Y. Rong: *Metall. Mater. Trans. A*, 2015, vol. 46A, pp. 4047–55. <https://doi.org/10.1007/s11661-015-3021-2>.
65. S. Barella, M. Belfi, A. Gruttadauria, C. Liu, and Y. Peng: *Metall. Mater. Trans. A*, 2024, vol. 55A, pp. 513–22. <https://doi.org/10.1007/s11661-023-07262-y>.

Publisher's Note Springer Nature remains neutral with regard to jurisdictional claims in published maps and institutional affiliations.

Springer Nature or its licensor (e.g. a society or other partner) holds exclusive rights to this article under a publishing agreement with the author(s) or other rightsholder(s); author self-archiving of the accepted manuscript version of this article is solely governed by the terms of such publishing agreement and applicable law.